Available online at www.sciencedirect.com

SCIENCE DIRECT®

Comput. Methods Appl. Mech. Engrg. 193 (2004) 3837–3870

Computer methods in applied mechanics and engineering

www.elsevier.com/locate/cma

Dynamics of porous media at finite strain

Chao Li [a], Ronaldo I. Borja [a,*,1], Richard A. Regueiro [b]

[a] *Department of Civil and Environmental Engineering, Stanford University, Stanford, CA 94305-4020, USA*
[b] *Department of Science-Based Materials Modeling, Sandia National Laboratories, Livermore, CA 94551, USA*

Received 20 November 2003; received in revised form 11 February 2004; accepted 12 February 2004

Abstract

We present a finite element model for the analysis of a mechanical phenomenon involving dynamic expulsion of fluids from a fully saturated porous solid matrix in the regime of large deformation. Momentum and mass conservation laws are written in Lagrangian form by a pull-back from the current configuration to the reference configuration following the solid matrix motion. A complete formulation based on the motion of the solid and fluid phases is first presented; then approximations are made with respect to the material time derivative of the relative flow velocity vector to arrive at a so-called $(\boldsymbol{v}, p)$-formulation, which is subsequently implemented in a finite element model. We show how the resulting finite element matrix equations can be consistently linearized, using a compressible neo-Hookean hyperelastic material with a Kelvin solid viscous enhancement for the solid matrix as a test function for the nonlinear constitutive model. Numerical examples are presented demonstrating the significance of large deformation effects on the transient dynamic responses of porous structures, as well as the strong convergence profile exhibited by the iterative algorithm.

Keywords: Dynamics; Porous media; Finite strain

---

1. Introduction

Porous media consist of a solid phase, usually referred to as a matrix or skeleton, as well as closed and open pores. Examples of porous materials are soils, rocks, the human bone, and porous aluminum foam, to name a few. The mechanics of porous media is of utmost relevance in many disciplines in engineering and science, such as geotechnical engineering, biomechanics, physical chemistry, agricultural engineering, and materials science. In geotechnical earthquake engineering, multiphase dynamics plays a major role in the prediction of the local site response where the buildup of fluid pressure induced by seismic shaking could

---

[*] Corresponding author. Address: Department of Civil and Environmental Engineering, Stanford University, Stanford, CA 94305-4020, USA. Fax: +1-650-723-7514.
E-mail address: borja@stanford.edu (R.I. Borja).

[1] Supported by NSF Grant No. CMS-02-01317.

doi:10.1016/j.cma.2004.02.014

lead to a rapid loss of strength of the saturated soil deposit, a phenomenon commonly referred to in the literature as liquefaction [1].

In biomechanics, multiphase dynamics is essential to hard and soft tissue growth and remodeling as cyclic stresses applied to the tissue solid/fluid mixture generate solid deformation, resulting in fluid flow and mass transport through the tissue solid matrix leading to cell nutrition, breakdown, and regeneration [2–5]. Multiphase dynamics also plays a significant role during head impacts as skull and brain tissues contact and deform with concomitant fluid flow in and out of the tissues [6]. Although deformation of bone is small (0.4% strain [7]), a geometrically nonlinear theory is needed in order to account properly for large rotations and translations experienced during dynamic loading such as head impact and knee bending. The finite deformation theory is also necessary for modeling contact of hard tissue with soft tissue (e.g., skull with brain, bone with cartilage, etc.) and resulting fluid flow. With regard to multi-phase continuum formulations in biomechanics, two- and three-field formulations (and more fields when chemical and electrical effects are included) have been used for simulating deformation of soft, hydrated biological tissues, such as cartilage and heart muscle, for small strains [8] and finite strains [9–15].

In geomechanics, multiphase finite element formulations of coupled deformation-fluid flow in porous media abound in the literature, but a majority of them ignore the effects of solid and fluid accelerations [16–23]. In the absence of inertia terms the coupled problem is of parabolic type, and the so-called $(\boldsymbol{v}, p)$-formulation is complete (where $\boldsymbol{v} =$ solid velocity field and $p =$ fluid pressure). Large deformation formulations are available for this type of problem [24–28]. For partially saturated media a three-phase $(\boldsymbol{v}, p_{\mathrm{w}}, p_{\mathrm{a}})$-approach offers a direct extension of the two-phase formulation [1,29–31] (where $p_{\mathrm{w}} =$ pore water pressure and $p_{\mathrm{a}} =$ pore air pressure).

In the presence of inertia terms the coupled problem is of hyperbolic type, and the so-called $(\boldsymbol{v}, p)$-formulation is no longer complete. Many authors [1,32–37] have shown that for this class of problem it is necessary to specify not only the motion of the solid phase but also that of the fluid phase to completely formulate the governing partial differential equations (PDEs). This can be achieved by specifying, for example, the fluid velocity field $\boldsymbol{v}_{\mathrm{f}}$, or, alternately, the relative flow velocity vector $\tilde{\boldsymbol{v}} = \boldsymbol{v}_{\mathrm{f}} - \boldsymbol{v}$, in addition to the solid velocity field $\boldsymbol{v}$, resulting in so-called $(\boldsymbol{v}, \boldsymbol{v}_{\mathrm{f}})$- and $(\boldsymbol{v}, \tilde{\boldsymbol{v}})$-formulations, respectively. The Lagrange multipliers method is sometimes used for ease in the solution process, leading to either the $(\boldsymbol{v}, \boldsymbol{v}_{\mathrm{f}}, p)$- or the $(\boldsymbol{v}, \tilde{\boldsymbol{v}}, p)$-formulation.

Whereas the solution techniques for the hyperbolic PDE for porous media have developed rapidly over the last decade, most deal only with infinitesimal deformations with the exception of a few. Large deformation formulations based on a hypoelastic theory are subject to criticisms that include, among others, the fact that it assumes negligible elastic deformations and that a unique objective stress rate cannot be possibly defined [38]. In addition, the hypoelastic formulation does not conveniently accommodate the commonly used return mapping algorithm in computational plasticity.

In this paper, we revisit the governing hyperbolic PDEs for fully saturated porous media and write them out in a form that accommodates the effects of finite deformation. The goal of the paper is to present a framework that can eventually be used to cast finite deformation multiplicative plasticity models. Thus, we follow the motion of the solid skeleton in a Lagrangian description and write the momentum balance equations using this description. The mass balance equations may be interpreted to provide volume constraints to the governing PDEs; by following the motion of the solid phase, we then write the mass balance equations identifying the spatial point as the instantaneous material point now occupied by the solid phase. It is noted that it would be very difficult and impractical to write the mass balance equation for the fluid phase Lagrangian point of view since this would require that we identify and follow the motion of the fluid material point.

For the hyperbolic problem we write the complete governing PDEs in $(\boldsymbol{v}, \boldsymbol{v}_{\mathrm{f}})$-form. By assuming that the material time derivative of the relative velocity vector $\tilde{\boldsymbol{v}}$ is zero, we arrive at the reduced $(\boldsymbol{v}, p)$-form, and this is what we then use in the finite element formulation. As noted in [1,32], this approximation is acceptable in the low-frequency range such as that encountered in geotechnical earthquake engineering applications. We then develop finite element matrix equations in residual form and linearize them consistently for iteration with Newton's method.

For the porous solid matrix we use a compressible neo-Hookean hyperelastic material model [39] enhanced with a Kelvin viscous solid [40]. The choice of this relatively simple material model allows us to focus more on the formulation and performance of the finite deformation model. Multiplicative plasticity models are based upon the framework of hyperelasticity [41], so they can easily be cast within the proposed finite deformation framework. To demonstrate the performance of the resulting finite element model, we present a number of numerical examples in 1D and 2D comparing the infinitesimal and finite deformation solutions as well as demonstrating the performance of the iterative solutions.

As for notations and symbols, bold-face letters denote matrices and vectors; the symbol '$\cdot$' denotes an inner product of two vectors (e.g., $\boldsymbol{a}\cdot\boldsymbol{b} = a_i b_i$), or a single contraction of adjacent indices of two tensors (e.g., $\boldsymbol{c}\cdot\boldsymbol{d} = c_{ij}d_{jk}$); the symbol ':' denotes an inner product of two second-order tensors (e.g., $\boldsymbol{c}:\boldsymbol{d} = c_{ij}d_{ij}$), or a double contraction of adjacent indices of tensors of rank two and higher (e.g., $\boldsymbol{D}:\boldsymbol{C} = D_{IJKL}C_{KL}$); upper-case subscripts refer to material coordinates while lower-case subscripts refer to spatial coordinates.

2. Mass and momentum balance laws

We consider a two-phase mixture (see [42–52] for relevant background) composed of a solid matrix whose voids are continuous and completely filled with fluid. The solid matrix, or skeleton, plays a special role in the mathematical description in that it defines the volume of the mixture, herein written in the current configuration as $V = V_s + V_f$. The corresponding total masses are $M = M_s + M_f$, where $M_\alpha = \rho_\alpha V_\alpha$ for $\alpha =$ solid and fluid; and ρ_α is the true mass density of the α phase. The volume fraction occupied by the α phase is given by $\phi^\alpha = V_\alpha / V$, and thus

$$\phi^s + \phi^f = 1. \tag{2.1}$$

The partial mass density of the α phase is given by $\rho^\alpha = \phi^\alpha \rho_\alpha$, and thus

$$\rho^s + \rho^f = \rho, \tag{2.2}$$

where $\rho = M/V$ is the total mass density of the mixture. As a general notation, phase designations in superscripts pertain to average or partial quantities; and in subscripts to intrinsic or true quantities.

2.1. Balance of mass

In writing out the mass balance equations for a two-phase mixture, we focus on the current configuration of the mixture and describe the motions of the fluid phase relative to the motion of the solid phase. We denote the instantaneous intrinsic velocities of the solid and fluid phases by $\boldsymbol{v}$ and $\boldsymbol{v}_f$, respectively, and the total time-derivative following the solid phase motion by

$$\frac{d(\cdot)}{dt} = \frac{\partial(\cdot)}{\partial t} + \operatorname{grad}(\cdot)\cdot\boldsymbol{v}. \tag{2.3}$$

For future use we also introduce the operator $d^f(\cdot)/dt$, which denotes a material time derivative following the fluid phase motion and is related to the operator $d(\cdot)/dt$ via the relation

$$\frac{d^f(\cdot)}{dt} = \frac{d(\cdot)}{dt} + \operatorname{grad}(\cdot)\cdot\tilde{\boldsymbol{v}}, \quad \tilde{\boldsymbol{v}} = \boldsymbol{v}_f - \boldsymbol{v}. \tag{2.4}$$

Ignoring mass exchanges between the two phases, balance of mass for the solid and fluid phases then write

$$\frac{\mathrm{d}\rho^{\mathrm{s}}}{\mathrm{d}t} + \rho^{\mathrm{s}}\,\mathrm{div}(\boldsymbol{v}) = 0, \tag{2.5a}$$

$$\frac{\mathrm{d}\rho^{\mathrm{f}}}{\mathrm{d}t} + \rho^{\mathrm{f}}\,\mathrm{div}(\boldsymbol{v}) = -\mathrm{div}(\boldsymbol{q}), \tag{2.5b}$$

Here, $\boldsymbol{q}$ is the Eulerian relative flow vector of the fluid phase with respect to the solid matrix, given explicitly by the relations

$$\boldsymbol{q} = \rho^{\mathrm{f}}\tilde{\boldsymbol{v}}. \tag{2.6}$$

The flow vector $\boldsymbol{q}$ has the physical significance that its scalar product with the unit normal vector $\boldsymbol{v}$ to a unit surface area attached to the solid matrix is the mass flux j of the fluid phase relative to the solid matrix flowing across the same unit area, i.e.,

$$\boldsymbol{q} \cdot \boldsymbol{v} = j. \tag{2.7}$$

Based on this definition of $\boldsymbol{q}$, it therefore follows that (2.5b) gives $\mathrm{d}^{\mathrm{f}}\rho^{\mathrm{f}}/\mathrm{d}t + \rho^{\mathrm{f}}\mathrm{div}(\boldsymbol{v}_{\mathrm{f}}) = 0$. When interpreting (2.6), the porous skeleton volume is assumed to have an isotropic distribution of voids so that when it is sliced in any direction the area fractions are numerically equal to the volume fractions.

For barotropic flows the bulk modulus of the α phase can be defined as [53,54]

$$K_{\alpha} = \rho_{\alpha}\frac{\mathrm{d}p_{\alpha}}{\mathrm{d}\rho_{\alpha}}, \quad \alpha = \mathrm{s}, \mathrm{f}, \tag{2.8}$$

where p_{α} is the intrinsic Cauchy pressure in the α phase, i.e., the force acting on this phase per unit area of the same phase. The symbol $\mathrm{d}p_{\alpha}/\mathrm{d}\rho_{\alpha}$ is the ordinary total derivative following the assumption of the existence of a functional relationship of the form $f_{\alpha}(p_{\alpha}, \rho_{\alpha}) = 0$ for each phase. The mass balance equations then become

$$\frac{\mathrm{d}\phi^{\mathrm{s}}}{\mathrm{d}t} + \frac{\phi^{\mathrm{s}}}{K_{\mathrm{s}}}\frac{\mathrm{d}p_{\mathrm{s}}}{\mathrm{d}t} + \phi^{\mathrm{s}}\,\mathrm{div}(\boldsymbol{v}) = 0, \tag{2.9a}$$

$$\frac{\mathrm{d}\phi^{\mathrm{f}}}{\mathrm{d}t} + \frac{\phi^{\mathrm{f}}}{K_{\mathrm{f}}}\frac{\mathrm{d}p_{\mathrm{f}}}{\mathrm{d}t} + \phi^{\mathrm{f}}\,\mathrm{div}(\boldsymbol{v}) = -\frac{1}{\rho_{\mathrm{f}}}\,\mathrm{div}(\boldsymbol{q}). \tag{2.9b}$$

Adding the last two equations and noting that $\phi^{\mathrm{s}} + \phi^{\mathrm{f}} = 1$ gives the Eulerian form of balance of mass

$$\frac{\phi^{\mathrm{s}}}{K_{\mathrm{s}}}\frac{\mathrm{d}p_{\mathrm{s}}}{\mathrm{d}t} + \frac{\phi^{\mathrm{f}}}{K_{\mathrm{f}}}\frac{\mathrm{d}p_{\mathrm{f}}}{\mathrm{d}t} + \mathrm{div}(\boldsymbol{v}) = -\frac{1}{\rho_{\mathrm{f}}}\,\mathrm{div}(\boldsymbol{q}). \tag{2.10}$$

Now, let $\boldsymbol{F} = \partial\boldsymbol{\phi}/\partial\boldsymbol{X}$ be the deformation gradient of the solid phase motion and $J = \det(\boldsymbol{F})$ be the Jacobian, with $\boldsymbol{\phi}$ and $\boldsymbol{X}$ being equal, respectively, to the coordinates in the current and reference configurations of the material point X contained in the solid matrix. Thus,

$$\boldsymbol{Q} = J\boldsymbol{F}^{-1} \cdot \boldsymbol{q} \tag{2.11}$$

is the Piola transform of $\boldsymbol{q}$, and

$$\mathrm{DIV}(\boldsymbol{q}) = J\,\mathrm{div}(\boldsymbol{q}) \tag{2.12}$$

is the Piola identity [55]. In (2.12), DIV is the divergence operator evaluated with respect to the reference solid phase coordinates.

Multiplying both sides of (2.10) by the Jacobian J, and noting that

$$J\frac{\mathrm{d}p_\alpha}{\mathrm{d}t}=\frac{\mathrm{d}(Jp_\alpha)}{\mathrm{d}t}-p_\alpha\frac{\mathrm{d}J}{\mathrm{d}t},\quad \alpha=\mathrm{s},\mathrm{f}, \tag{2.13}$$

we get

$$\frac{\phi^{\mathrm{s}}}{K_{\mathrm{s}}}\frac{\mathrm{d}\theta_{\mathrm{s}}}{\mathrm{d}t}+\frac{\phi^{\mathrm{f}}}{K_{\mathrm{f}}}\frac{\mathrm{d}\theta_{\mathrm{f}}}{\mathrm{d}t}+\left[1-\frac{\phi^{\mathrm{s}}p_{\mathrm{s}}}{K_{\mathrm{s}}}-\frac{\phi^{\mathrm{f}}p_{\mathrm{f}}}{K_{\mathrm{f}}}\right]\frac{\mathrm{d}J}{\mathrm{d}t}=-\frac{1}{\rho_{\mathrm{f}}}\mathrm{DIV}(\boldsymbol{Q}), \tag{2.14}$$

where

$$\theta_{\mathrm{s}}=Jp_{\mathrm{s}},\quad \theta_{\mathrm{f}}=Jp_{\mathrm{f}} \tag{2.15}$$

are the Kirchhoff mean solid pressure and pore fluid pressure, respectively. We note that in the limit of incompressible solid and fluid phases, we easily recover the relation (see [25])

$$\frac{\mathrm{d}J}{\mathrm{d}t}+\frac{1}{\rho_{\mathrm{f}}}\mathrm{DIV}(\boldsymbol{Q})=0. \tag{2.16}$$

Fig. 1 shows the motions of the solid and fluid phases. Note that the fluid now occupying the void at a point $\varphi(X,t)$, where φ is the motion of the solid phase and X is a material point attached to the solid matrix, is not necessarily the same fluid material that occupied the same void at a reference point $\varphi(X,0)$. Thus, the total mass of the solid–fluid mixture is not necessarily conserved by the motion of the solid matrix, see [25] for an elaboration of this point.

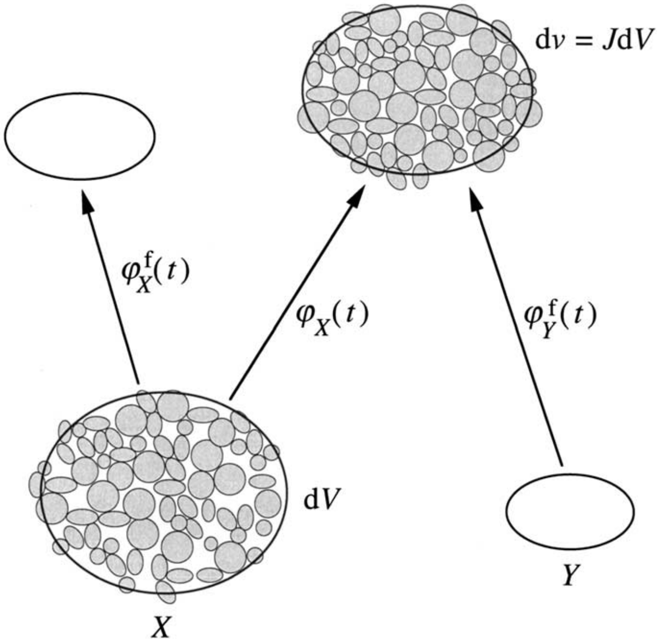

Fig. 1. Balance of mass: solid and fluid phase motions are described by trajectories $\varphi_X(t)$ and $\varphi_X^{(\mathrm{f})}(t)$. Fluid at X leaves $\mathrm{d}V$ while fluid initially at Y enters $\mathrm{d}v$ at time t.

2.2. Balance of momentum

Let $\boldsymbol{\sigma}^\alpha$ denote the Cauchy partial stress tensor for the α phase, with $\alpha =$ solid and fluid. The total Cauchy stress tensor $\boldsymbol{\sigma}$ is obtained from the sum

$$\boldsymbol{\sigma} = \boldsymbol{\sigma}^{\mathrm{s}} + \boldsymbol{\sigma}^{\mathrm{f}}. \tag{2.17}$$

This decomposition of the total Cauchy stress tensor readily provides expressions for the intrinsic Cauchy pressures p_{s} and p_{f} as follows:

$$p_{\mathrm{s}} = -\frac{1}{3\phi^{\mathrm{s}}}\mathrm{tr}(\boldsymbol{\sigma}^{\mathrm{s}}), \quad p_{\mathrm{f}} = -\frac{1}{3\phi^{\mathrm{f}}}\mathrm{tr}(\boldsymbol{\sigma}^{\mathrm{f}}). \tag{2.18}$$

Thus, if $\boldsymbol{\sigma}^{\mathrm{f}}$ is an isotropic tensor of the form $\boldsymbol{\sigma}^{\mathrm{f}} = \beta\mathbf{1}$, then $\beta = -\phi^{\mathrm{f}} p_{\mathrm{f}} = -p^{\mathrm{f}}$.

Now, defining the corresponding first Piola–Kirchhoff partial stress tensor as $\boldsymbol{P}^\alpha = J\boldsymbol{\sigma}^\alpha \cdot \boldsymbol{F}^{-\mathrm{t}}$, the total first Piola–Kirchhoff stress tensor is then given by

$$\boldsymbol{P} = \boldsymbol{P}^{\mathrm{s}} + \boldsymbol{P}^{\mathrm{f}}. \tag{2.19}$$

By mixture theory, balance of linear momentum for the α phase may be expressed through the alternative equations

$$\mathrm{div}(\boldsymbol{\sigma}^\alpha) + \rho^\alpha \mathbf{g} + \boldsymbol{h}^\alpha = \rho^\alpha \frac{\mathrm{d}^\alpha \boldsymbol{v}_\alpha}{\mathrm{d}t}, \tag{2.20a}$$

$$\mathrm{DIV}(\boldsymbol{P}^\alpha) + J\rho^\alpha \mathbf{g} + \boldsymbol{H}^\alpha = J\rho^\alpha \frac{\mathrm{d}^\alpha \boldsymbol{v}_\alpha}{\mathrm{d}t}, \tag{2.20b}$$

for $\alpha =$ solid and fluid; where $\boldsymbol{v}_{\mathrm{s}} \equiv \boldsymbol{v}$ and $\mathrm{d}^{\mathrm{s}}(\cdot)/\mathrm{d}t \equiv \mathrm{d}(\cdot)/\mathrm{d}t$; $\mathbf{g}$ is the vector of gravity accelerations; $\boldsymbol{h}^\alpha$ is the resultant body force per unit current volume of the solid matrix exerted on the α phase; $\boldsymbol{H}^\alpha = J\boldsymbol{h}^\alpha$ is the corresponding resultant body force per unit reference volume of the solid matrix; and 'div' and 'DIV' are the divergence operators evaluated with respect to the current and reference configurations, respectively. The forces $\boldsymbol{h}^\alpha$ and $\boldsymbol{H}^\alpha$ are internal to the mixture and thus satisfy the relations $\boldsymbol{h}^{\mathrm{s}} + \boldsymbol{h}^{\mathrm{f}} = \boldsymbol{H}^{\mathrm{s}} + \boldsymbol{H}^{\mathrm{f}} = \mathbf{0}$.

Adding (2.20) for the two phases, we obtain the balance of momentum for the entire mixture expressed in the alternative forms

$$\mathrm{div}(\boldsymbol{\sigma}) + \rho \mathbf{g} = \sum_{\alpha=\mathrm{s,f}} \rho^\alpha \frac{\mathrm{d}^\alpha \boldsymbol{v}_\alpha}{\mathrm{d}t}, \tag{2.21a}$$

$$\mathrm{DIV}(\boldsymbol{P}) + \rho_0 \mathbf{g} = \sum_{\alpha=\mathrm{s,f}} J\rho^\alpha \frac{\mathrm{d}^\alpha \boldsymbol{v}_\alpha}{\mathrm{d}t}, \tag{2.21b}$$

where $\rho_0 = J\rho$ is the pull-back mass density of the mixture in the reference configuration. We note that the solid phase material now at point $\boldsymbol{x}$ in the current configuration is the same solid phase material originally at the point $\boldsymbol{X}$ in the reference configuration, but the fluids at $\boldsymbol{x}$ and $\boldsymbol{X}$ are not the same material points. Hence, the total reference mass density ρ_0 in V_0 is not conserved by ρ in V.

We now define material acceleration vectors

$$\boldsymbol{a} := \frac{\mathrm{d}\boldsymbol{v}}{\mathrm{d}t}, \quad \boldsymbol{a}_{\mathrm{f}} := \frac{\mathrm{d}^{\mathrm{f}} \boldsymbol{v}_{\mathrm{f}}}{\mathrm{d}t}, \quad \widetilde{\boldsymbol{a}} := \boldsymbol{a}_{\mathrm{f}} - \boldsymbol{a}. \tag{2.22}$$

Clearly, $\boldsymbol{a}$ is the material acceleration of the solid phase, while $\widetilde{\boldsymbol{a}}$ is the relative material acceleration of the fluid phase to the solid phase. The latter acceleration can be written in alternative forms

$$\widetilde{\boldsymbol{a}} = \frac{\mathrm{d}\tilde{\boldsymbol{v}}}{\mathrm{d}t} + \mathrm{grad}(\boldsymbol{v}_{\mathrm{f}}) \cdot \tilde{\boldsymbol{v}}, \tag{2.23a}$$

$$= \frac{\partial\tilde{\boldsymbol{v}}}{\partial t} + \mathrm{grad}(\boldsymbol{v}_{\mathrm{f}}) \cdot \boldsymbol{v}_{\mathrm{f}} - \mathrm{grad}(\boldsymbol{v}) \cdot \boldsymbol{v}. \tag{2.23b}$$

Rewriting (2.21), we then get

$$\mathrm{div}(\boldsymbol{\sigma}) + \rho\mathbf{g} = \rho\boldsymbol{a} + \rho^{\mathrm{f}}\widetilde{\boldsymbol{a}}, \tag{2.24a}$$

$$\mathrm{DIV}(\boldsymbol{P}) + \rho_0\mathbf{g} = \rho_0\boldsymbol{a} + J\rho^{\mathrm{f}}\widetilde{\boldsymbol{a}}. \tag{2.24b}$$

2.3. Complete and simplified formulations

The relations presented in the previous section, combined with suitable constitutive assumptions, constitute a complete $(\boldsymbol{v}, \boldsymbol{v}_{\mathrm{f}})$-formulation of the hyperbolic solid deformation-diffusion problem. To demonstrate the completeness of the formulation, one can write the balance of momentum for the total mixture and the balance of momentum for the fluid phase,

$$\mathrm{div}(\boldsymbol{\sigma}) + \rho\mathbf{g} = \rho\boldsymbol{a} + \rho^{\mathrm{f}}\widetilde{\boldsymbol{a}}, \tag{2.25a}$$

$$-\mathrm{grad}(\phi^{\mathrm{f}}p_{\mathrm{f}}) + \rho^{\mathrm{f}}\mathbf{g} + \boldsymbol{h}^{\mathrm{f}} = \rho^{\mathrm{f}}\boldsymbol{a}_{\mathrm{f}}. \tag{2.25b}$$

The assumption of barotropic flow determines the intrinsic mass densities ρ_{s} and ρ_{f} from the intrinsic pressures p_{s} and p_{f}. With suitable constitutive assumptions the evolutions of $\boldsymbol{\sigma}$, $\boldsymbol{h}^{\mathrm{f}}$, and p_{s} can be related to the evolutions of $\boldsymbol{v}$ and $\boldsymbol{v}_{\mathrm{f}}$ and the void fractions. The evolution of the solid volume fraction ϕ^{s} is determined from balance of mass for the solid phase, (2.9a),

$$\frac{1}{\phi^{\mathrm{s}}}\frac{\mathrm{d}\phi^{\mathrm{s}}}{\mathrm{d}t} = -\frac{1}{K_{\mathrm{s}}}\frac{\mathrm{d}p_{\mathrm{s}}}{\mathrm{d}t} - \mathrm{div}(\boldsymbol{v}), \tag{2.26a}$$

which in turn determines the evolution of the fluid volume fraction $\phi^{\mathrm{f}} = 1 - \phi^{\mathrm{s}}$. Thus, (2.25) constitutes six equations in the unknowns $\boldsymbol{v}$, $\boldsymbol{v}_{\mathrm{f}}$ and the intrinsic fluid pressure p_{f}. The latter unknown is solved from balance of mass for the fluid phase, (2.9b),

$$\frac{\mathrm{d}p_{\mathrm{f}}}{\mathrm{d}t} = -K_{\mathrm{f}}\left[\frac{1}{\phi_{\mathrm{f}}}\frac{\mathrm{d}\phi^{\mathrm{f}}}{\mathrm{d}t} + \mathrm{div}(\boldsymbol{v}) + \frac{1}{\rho^{\mathrm{f}}}\mathrm{div}(\boldsymbol{q})\right], \tag{2.26b}$$

where $\boldsymbol{q}$ is also related to $\boldsymbol{v}$ and $\boldsymbol{v}_{\mathrm{f}}$ from the field equations. Thus, in principle all of the variables can be expressed in terms of $\boldsymbol{v}$ and $\boldsymbol{v}_{\mathrm{f}}$, and thus, with suitable constitutive assumptions the $(\boldsymbol{v}, \boldsymbol{v}_{\mathrm{f}})$-formulation is complete.

If the relative acceleration $\widetilde{\boldsymbol{a}}$ is ignored, then we recover the simplified $(\boldsymbol{v}, p)$-formulation. The governing equations are obtained from imposing balance of momentum and balance of mass for the total mixture as

$$\mathrm{div}(\boldsymbol{\sigma}) + \rho\mathbf{g} = \rho\boldsymbol{a}, \tag{2.27}$$

$$\frac{\phi^{\mathrm{s}}}{K_{\mathrm{s}}}\frac{\mathrm{d}p_{\mathrm{s}}}{\mathrm{d}t} + \frac{\phi^{\mathrm{f}}}{K_{\mathrm{f}}}\frac{\mathrm{d}p_{\mathrm{f}}}{\mathrm{d}t} + \mathrm{div}(\boldsymbol{v}) = -\frac{1}{\rho_{\mathrm{f}}}\mathrm{div}(\boldsymbol{q}). \tag{2.28}$$

Alternative expressions are

$$\mathrm{DIV}(\boldsymbol{P}) + \rho_0\mathbf{g} = \rho_0\boldsymbol{a}, \tag{2.29}$$

$$\frac{\phi^{\mathrm{s}}}{K_{\mathrm{s}}}\frac{\mathrm{d}\theta_{\mathrm{s}}}{\mathrm{d}t} + \frac{\phi^{\mathrm{f}}}{K_{\mathrm{f}}}\frac{\mathrm{d}\theta_{\mathrm{f}}}{\mathrm{d}t} + \left[1 - \frac{\phi^{\mathrm{s}}p_{\mathrm{s}}}{K_{\mathrm{s}}} - \frac{\phi^{\mathrm{f}}p_{\mathrm{f}}}{K_{\mathrm{f}}}\right]\frac{\mathrm{d}J}{\mathrm{d}t} = -\frac{1}{\rho_{\mathrm{f}}}\mathrm{DIV}(\boldsymbol{Q}). \tag{2.30}$$

2.4. Constitutive assumptions

To complete the mathematical description of the problem, a constitutive relation for the mechanical deformation of the solid matrix and a constitutive relation for fluid flow in the dynamic regime must be specified. For the deformation of the solid matrix the constitutive relation may be formulated in terms of the partial stress tensor $\boldsymbol{P}^{\mathrm{s}}$ introduced in Section 2.2. Alternately, other suitable energy-conjugate relations may be utilized, such as the effective stress tensor $\boldsymbol{P}'$ that is energy-conjugate to $\dot{\boldsymbol{F}}$, the rate of the deformation gradient tensor (see [30,50]). Following Terzaghi's [56] idea, the effective stress equation may be written in the alternative forms [25]

$$\boldsymbol{P} = \boldsymbol{P}' - \theta \boldsymbol{F}^{-\mathrm{t}}, \quad \boldsymbol{S} = \boldsymbol{S}' - \theta \boldsymbol{C}^{-1}, \quad \boldsymbol{\tau} = \boldsymbol{\tau}' - \theta \mathbf{1}, \tag{2.31}$$

where the effective (primed) stress tensors are given by the relations $\boldsymbol{S}' = \boldsymbol{F}^{-1} \cdot \boldsymbol{P}' = \boldsymbol{F}^{-1} \cdot \boldsymbol{\tau}' \cdot \boldsymbol{F}^{-\mathrm{t}}$ (the general symbols $\boldsymbol{P}$ and $\boldsymbol{S}$ refer to the first and second Piola–Kirchhoff stress tensors, respectively), and $\boldsymbol{C} = \boldsymbol{F}^{\mathrm{t}} \cdot \boldsymbol{F}$ is the right Cauchy–Green deformation tensor.

For the effective stress tensor $\boldsymbol{S}'$, we postulate an additive decomposition of the form

$$\boldsymbol{S}' = \boldsymbol{S}'_{\mathrm{inv}} + \boldsymbol{S}'_{\mathrm{vis}}, \tag{2.32}$$

where $\boldsymbol{S}'_{\mathrm{inv}}$ and $\boldsymbol{S}'_{\mathrm{vis}}$ are the inviscid and viscous parts of $\boldsymbol{S}'$, respectively. For the inviscid part we consider a compressible neo-Hookean hyperelastic material based the stored energy function [39]

$$\Psi(\boldsymbol{X}, \boldsymbol{C}) = \frac{\mu}{2}[\mathrm{tr}(\boldsymbol{C}) - 3] - \mu \ln J + \frac{\lambda}{2}(\ln J)^2, \tag{2.33}$$

where λ and μ are the Lamé constants, and $J = \sqrt{I_{3C}}$ is the square-root of the third invariant of the deformation tensor $\boldsymbol{C}$. This gives

$$\boldsymbol{S}'_{\mathrm{inv}} = 2\frac{\partial \Psi}{\partial \boldsymbol{C}} = \mu \mathbf{1} + (\lambda \ln J - \mu)\boldsymbol{C}^{-1}. \tag{2.34}$$

Frame-indifference of $\boldsymbol{S}'_{\mathrm{inv}}$, or invariance under superposed spatial rigid body motions, is guaranteed by having Ψ vary with deformation through the tensor $\boldsymbol{C}$.

For the viscous part we consider a Kelvin solid [38,40] and postulate the following form for $\boldsymbol{S}'_{\mathrm{vis}}$:

$$\boldsymbol{S}'_{\mathrm{vis}} = \alpha \mathsf{C} : \left(\tfrac{1}{2}\dot{\boldsymbol{C}}\right), \tag{2.35}$$

where α is a parameter reflecting the viscous damping characteristics of the solid matrix, and C is the second tangential elasticity tensor which takes the form

$$\mathsf{C} = 4\frac{\partial^2 \Psi}{\partial \boldsymbol{C} \partial \boldsymbol{C}} = \lambda \boldsymbol{C}^{-1} \otimes \boldsymbol{C}^{-1} + 2(\mu - \lambda \ln J)\boldsymbol{I}_{C^{-1}}, \tag{2.36}$$

where $\boldsymbol{I}_{C^{-1}} = \partial(\boldsymbol{C}^{-1})/\partial \boldsymbol{C}$ is a rank-four tensor with components $(I_{C^{-1}})_{IJKL} = (C^{-1}_{IK}C^{-1}_{JL} + C^{-1}_{IL}C^{-1}_{JK})/2$. Note that this form for $\boldsymbol{I}_{C^{-1}}$ differs from that reported in [39] for this particular model, which did not correctly reflect the minor symmetry of $\boldsymbol{I}_{C^{-1}}$. Applying a push-forward on all four indices of C gives the fourth-order spatial tangential elasticity tensor c with components

$$\mathsf{c}_{ijkl} = F_{iI}F_{jJ}F_{kK}F_{lL}\mathsf{C}_{IJKL} \Rightarrow \mathsf{C} = \lambda' \mathbf{1} \otimes \mathbf{1} + 2\mu' \boldsymbol{I}, \quad \lambda' = \lambda, \quad \mu' = \mu - \lambda \ln J, \tag{2.37}$$

where λ' and μ' are the equivalent Lamé constants, and $\boldsymbol{I}$ is a rank-four identity tensor with components $I_{ijkl} = (\delta_{ik}\delta_{jl} + \delta_{il}\delta_{jk})/2$. The choice of the above form for the viscous component of stress is motivated in great part by its invariance under superposed spatial rigid body motions, which follows by having C vary with deformation through the tensor $\boldsymbol{C}$ and by the fact that $\dot{\boldsymbol{C}}$ is frame indifferent as well.

For fluid flow in the dynamic regime the constitutive equation relates the internal body force vector $\boldsymbol{h}^{\mathrm{f}}$ to the Eulerian relative flow vector $\boldsymbol{q}$ via [1,33]

$$\boldsymbol{h}^{\mathrm{f}} = \phi^{\mathrm{f}}\rho_{\mathrm{f}}g\boldsymbol{k}^{-1}\cdot\phi^{\mathrm{f}}(\boldsymbol{v}_{\mathrm{f}} - \boldsymbol{v}) = \phi^{\mathrm{f}}g\boldsymbol{k}^{-1}\cdot\boldsymbol{q}, \tag{2.38}$$

where $\boldsymbol{k}$ is a symmetric, positive-definite second-order tensor of hydraulic conductivities. We recall that $\boldsymbol{h}^{\mathrm{f}}$ is a body force per unit current volume representing the exchange of momentum between the solid and fluid constituents. Substituting into the balance of momentum for the fluid phase, (2.25b), and solving for $\boldsymbol{q}$ gives

$$\boldsymbol{q} = \rho_{\mathrm{f}}\boldsymbol{k}\cdot\left[\frac{1}{\phi^{\mathrm{f}}\rho_{\mathrm{f}}g}\operatorname{grad}\left(\frac{\phi^{\mathrm{f}}\theta}{J}\right) + \frac{\boldsymbol{a} - \mathbf{g}}{g}\right]. \tag{2.39}$$

This is the generalized form of Darcy's law in the dynamic regime, evident from the presence of the acceleration vector $\boldsymbol{a}$ (we recall that this vector should have been the material acceleration of the fluid phase, $\boldsymbol{a}_{\mathrm{f}}$, which has now been replaced by the solid matrix acceleration $\boldsymbol{a}$ in light of the assumption that the relative acceleration vector $\widetilde{\boldsymbol{a}}$ is negligible).

Following [25], the Piola transform of $\boldsymbol{q}$ is given by

$$\boldsymbol{Q} = J\boldsymbol{F}^{-1}\cdot\boldsymbol{q} = \rho_{\mathrm{f}}\boldsymbol{k}'\cdot\left[\frac{1}{\phi^{\mathrm{f}}\rho_{\mathrm{f}}g}\operatorname{grad}\left(\frac{\phi^{\mathrm{f}}\theta}{J}\right) + \frac{\boldsymbol{a} - \mathbf{g}}{g}\right], \tag{2.40}$$

where $\boldsymbol{k}' = J\boldsymbol{F}^{-1}\cdot\boldsymbol{k}$ is a two-point hydraulic conductivity tensor with components k'_{Ij} relating the fluid mass flux in the reference configuration of the solid matrix to the relative fluid velocity at the same material point in the current configuration. Alternately, we can also pull back the second index of $\boldsymbol{k}'$ and write the Piola transform $\boldsymbol{Q}$ as [25]

$$\boldsymbol{Q} = \rho_{\mathrm{f}}\boldsymbol{K}\cdot\left[\frac{1}{\phi^{\mathrm{f}}\rho_{\mathrm{f}}g}\operatorname{GRAD}\left(\frac{\phi^{\mathrm{f}}\theta}{J}\right) + \boldsymbol{F}^{\mathrm{t}}\cdot\frac{\boldsymbol{a} - \mathbf{g}}{g}\right], \tag{2.41}$$

where $\boldsymbol{K} = J\boldsymbol{F}^{-1}\cdot\boldsymbol{k}\cdot\boldsymbol{F}^{-\mathrm{t}}$ is a pull-back hydraulic conductivity tensor with components K_{IJ} relating the pull backs of both the fluid mass flux and the relative fluid velocity vectors from the current to reference configurations of the solid matrix. The above expressions allow the formulation of the variational equations for momentum and mass balance with respect to both reference and current configurations.

3. Finite element formulation

In this section we present a finite element formulation for the hyperbolic solid deformation-diffusion problem. Here, we use the simplified $(\boldsymbol{v}, p)$-formulation. Furthermore, we assume the solid phase to be incompressible, $K_{\mathrm{s}} \to \infty$, which is a physically reasonable assumption in most geomechanics applications. Finally, we also assume that the intrinsic pressure p_{f} is much smaller than the fluid bulk modulus K_{f}. For water with a bulk modulus of 2.2×10^{7} kPa [57], the fluid pressure p_{f} can reach this order of magnitude at thousands of kilometers depth, so the latter assumption is valid in almost all applications. However, if the fluid itself is a mixture of liquid and gas, then the overall bulk modulus of the fluid mixture could be several orders of magnitude lower than the bulk modulus of the liquid alone due to the high compressibility of the gas voids [30], thus limiting the validity of the latter assumption. We note that $p_{\mathrm{f}}/K_{\mathrm{f}} \approx 0$ does not necessarily imply $\dot{p}_{\mathrm{f}}/K_{\mathrm{f}} \approx 0$ since the pore pressure can change quickly with time especially in a dynamic problem, so by this assumption we are not entirely neglecting the effect of fluid compressibility.

3.1. Strong form of the boundary-value problem

The strong form of the boundary-value problem is as follows. Let $\mathscr{B}$ be a simple body with boundary $\partial\mathscr{B}$ defined by the solid matrix in the reference configuration. We want to find the solid matrix deformation $\varphi : \mathscr{B} \rightarrow R^{n_{\mathrm{sd}}}$ and fluid pressure function $\theta : \mathscr{B} \rightarrow R^1$ (with $\theta \equiv \theta_{\mathrm{f}}$, dropping the subscript from now on) such that the following equations are satisfied:

$$\mathrm{DIV}(\boldsymbol{P}) + \rho_0 \mathbf{g} - \rho_0 \boldsymbol{a} = \mathbf{0} \quad \text{in } \mathscr{B}, \tag{3.1}$$

$$\frac{\rho^{\mathrm{f}}}{K_{\mathrm{f}}}\dot{\theta} + \rho_{\mathrm{f}}\dot{J} + \mathrm{DIV}(\boldsymbol{Q}) = 0 \quad \text{in } \mathscr{B}, \tag{3.2}$$

$$\varphi = \varphi_{\mathrm{d}} \quad \text{on } \partial\mathscr{B}^d, \tag{3.3}$$

$$\boldsymbol{P} \cdot \boldsymbol{N} = \boldsymbol{t} \quad \text{on } \partial\mathscr{B}^t, \tag{3.4}$$

$$\theta = \theta_{\mathrm{p}} \quad \text{on } \partial\mathscr{B}^p, \tag{3.5}$$

$$\boldsymbol{Q} \cdot \boldsymbol{N} = Q \quad \text{on } \partial\mathscr{B}^q, \tag{3.6}$$

where $\boldsymbol{a}$ is the material acceleration of the solid phase (also equal to the material acceleration of the fluid phase based on the assumption that $\tilde{\boldsymbol{a}} \approx \mathbf{0}$), φ_{d} and θ_{p} are prescribed solid matrix deformation and fluid pressure function, respectively (Dirichlet boundary conditions); and $\boldsymbol{t}$ and Q are prescribed nominal tractions and nominal fluid fluxes on a unit area with unit normal $\boldsymbol{N}$ in the undeformed solid matrix configuration, respectively (Neumann boundary conditions). For purposes of physical definition, $\theta = Jp_{\mathrm{f}}$ is the intrinsic Kirchhoff pore pressure function.

The initial conditions are

$$\varphi(\boldsymbol{X}, 0) = \varphi_0(\boldsymbol{X}), \quad \dot{\varphi}(\boldsymbol{X}, 0) = \dot{\varphi}_0(\boldsymbol{X}), \quad \theta(\boldsymbol{X}, 0) = \theta_0(\boldsymbol{X}), \quad \boldsymbol{X} \in \mathscr{B}. \tag{3.7}$$

The evolutions of the state variables are as follows. We assume a constant fluid bulk modulus K_{f} so that the intrinsic fluid mass density ρ_{f} varies with the intrinsic fluid pressure p_{f} according to

$$K_{\mathrm{f}} = \rho_{\mathrm{f}} \frac{\mathrm{d}p_{\mathrm{f}}}{\mathrm{d}\rho_{\mathrm{f}}} = \text{constant} \quad \Rightarrow \quad \rho_{\mathrm{f}} = \rho_{\mathrm{f0}} \exp\left(\frac{p_{\mathrm{f}} - p_{\mathrm{f0}}}{K_{\mathrm{f}}}\right), \tag{3.8}$$

where ρ_{f0} is the initial reference fluid mass density at initial fluid pressure p_{f0}. Balance of mass for the solid phase assuming $K_{\mathrm{s}} \rightarrow \infty$ reduces to $\dot{\phi}^{\mathrm{s}} + \phi^{\mathrm{s}}\,\mathrm{div}(\boldsymbol{v}) = 0$, which gives the evolution of the volume fractions as

$$\phi^{\mathrm{s}} = \phi^{\mathrm{s0}}/J, \quad \phi^{\mathrm{f}} = 1 - (1 - \phi^{\mathrm{f0}})/J, \tag{3.9}$$

where ϕ^{s0} and ϕ^{f0} are the reference values of ϕ^{s} and ϕ^{f} when $J = 1$. In the above descriptions the following usual boundary decompositions hold

$$\partial\mathscr{B} = \overline{\partial\mathscr{B}^d \cup \partial\mathscr{B}^t} = \overline{\partial\mathscr{B}^\theta \cup \partial\mathscr{B}^q}, \quad \partial\mathscr{B}^d \cap \partial\mathscr{B}^t = \partial\mathscr{B}^\theta \cap \partial\mathscr{B}^q = \emptyset, \tag{3.10}$$

where the overlines denote a closure. The overdots are used above in place of the material time derivative operator $\mathrm{d}(\cdot)/\mathrm{d}t$ since there is no ambiguity now that we only follow the motion of the solid phase.

3.2. Weak form

Following the standard arguments of variational principles, we define the following spaces. Let the space of configurations be

$$\mathscr{C}_\varphi = \{\varphi : \mathscr{B} \to R^{n_{\mathrm{sd}}} |\ \varphi_i \in H^1,\ \varphi = \varphi_{\mathrm{d}} \text{ on } \partial\mathscr{B}^d\}$$

and the space of variations be

$$\mathscr{V}_\varphi = \{\boldsymbol{\eta} : \mathscr{B} \to R^{n_{\mathrm{sd}}} \,|\, \eta_i \in H^1, \boldsymbol{\eta} = \mathbf{0} \text{ on } \partial\mathscr{B}^d\},$$

where H^1 is the usual Sobolev space of functions of degree one. Also, we define the space of pressure functions as

$$\mathscr{C}_\theta = \{\theta : \mathscr{B} \to R \,|\, \theta \in H^1, \theta = \theta_p \text{ on } \partial\mathscr{B}^p\}$$

and the corresponding space of variations as

$$\mathscr{V}_\theta = \{\psi : \mathscr{B} \to R \,|\, \psi \in H^1, \psi = 0 \text{ on } \partial\mathscr{B}^p\}.$$

Let $G : \mathscr{C}_\varphi \times \mathscr{C}_\theta \times \mathscr{V}_\varphi \to R$ be given by

$$G(\varphi, \theta, \boldsymbol{\eta}) = \int_{\mathscr{B}} (\mathrm{GRAD}\,\boldsymbol{\eta} : \boldsymbol{P} - \rho_0 \boldsymbol{\eta} \cdot \mathbf{g} + \rho_0 \boldsymbol{\eta} \cdot \boldsymbol{a}) \mathrm{d}V - \int_{\partial\mathscr{B}^t} \boldsymbol{\eta} \cdot \boldsymbol{t} \, \mathrm{d}A. \tag{3.11}$$

Then, balance of linear momentum is given by the condition $G(\varphi, \theta, \boldsymbol{\eta}) = 0$, which is equivalent to (3.1) if $\boldsymbol{P}$ and $\boldsymbol{\eta}$ are assumed to be C^1. Further, let $H : \mathscr{C}_\varphi \times \mathscr{C}_\theta \times \mathscr{V}_\theta \to R$ be given by

$$H(\varphi, \theta, \psi) = \int_{\mathscr{B}} \left(\psi \frac{\rho^{\mathrm{f}}}{K_{\mathrm{f}}} \dot{\theta} + \psi \rho_{\mathrm{f}} \dot{J} - \mathrm{GRAD}\,\psi \cdot \boldsymbol{Q} \right) \mathrm{d}V - \int_{\partial\mathscr{B}^q} \psi Q \, \mathrm{d}A. \tag{3.12}$$

Again, one can show that balance of mass is given by the condition $H(\varphi, \theta, \psi) = 0$, which is equivalent to (3.2) if ψ and θ are assumed to be C^1.

The weak form of the boundary-value problem is as follows. Find $\varphi \in \mathscr{C}_\varphi$ and $\theta \in \mathscr{C}_\theta$ such that

$$G(\varphi, \theta, \boldsymbol{\eta}) = H(\varphi, \theta, \psi) = 0 \tag{3.13}$$

for all $\boldsymbol{\eta} \in \mathscr{V}_\varphi$ and $\psi \in \mathscr{V}_\theta$.

Condition (3.13) emanates directly from the strong form of the boundary-value problem. We note that both G and H possess a Lagrangian form invoked by a pull back to the solid matrix reference configuration. The assumption of negligible relative acceleration allows us to capture the fluid degree of freedom in terms of the scalar field variable θ whose variation with time is described materially at a point attached to the solid matrix. From an implementational standpoint, this is crucial for developing mixed finite elements containing pressure and displacement nodes that move with the solid matrix, similar to those employed in the infinitesimal theory. For future reference, we note the following equivalent expressions

$$\int_{\mathscr{B}} \mathrm{GRAD}\,\boldsymbol{\eta} : \boldsymbol{P} \, \mathrm{d}V = \int_{\mathscr{B}} \mathrm{grad}\,\boldsymbol{\eta} : \boldsymbol{\tau} \, \mathrm{d}V = \int_{\varphi_t(\mathscr{B})} \mathrm{grad}\,\boldsymbol{\eta} : \boldsymbol{\sigma} \, \mathrm{d}v, \tag{3.14a}$$

$$\int_{\mathscr{B}} \mathrm{GRAD}\,\psi \cdot \boldsymbol{Q} \, \mathrm{d}V = \int_{\mathscr{B}} \mathrm{grad}\,\psi \cdot J\boldsymbol{q} \, \mathrm{d}V = \int_{\varphi_t(\mathscr{B})} \mathrm{grad}\,\psi \cdot \boldsymbol{q} \, \mathrm{d}v. \tag{3.14b}$$

As for the ‘internal virtual work,’ the first (stress) equation writes

$$\begin{aligned}\int_{\mathscr{B}} \mathrm{GRAD}\,\boldsymbol{\eta} : \boldsymbol{P}\,\mathrm{d}V &= \int_{\mathscr{B}} \mathrm{GRAD}\,\boldsymbol{\eta} : \boldsymbol{P}'_{\mathrm{inv}}\,\mathrm{d}V + \alpha \int_{\mathscr{B}} \mathrm{GRAD}\,\boldsymbol{\eta} : \left[\boldsymbol{F} \cdot \mathsf{C} : \left(\frac{1}{2}\dot{\boldsymbol{C}}\right)\right]\mathrm{d}V \\ &\quad - \int_{\mathscr{B}} \theta\,\mathrm{GRAD}\,\boldsymbol{\eta} : \boldsymbol{F}^{-\mathrm{t}}\,\mathrm{d}V = \int_{\mathscr{B}} \mathrm{grad}\,\boldsymbol{\eta} : \boldsymbol{\tau}'_{\mathrm{inv}}\,\mathrm{d}V \\ &\quad + \alpha \int_{\mathscr{B}} \mathrm{grad}\,\boldsymbol{\eta} : \mathsf{c} : \mathrm{grad}\,\boldsymbol{v}\,\mathrm{d}V - \int_{\mathscr{B}} \theta\,\mathrm{div}\,\boldsymbol{\eta}\,\mathrm{d}V, \end{aligned} \tag{3.15}$$

and we readily see a stiffness-proportional damping represented by the second integral on the right-hand side. The second (flow) equation writes

$$\begin{aligned}\int_{\mathscr{B}} \mathrm{GRAD}\,\psi \cdot \boldsymbol{Q}\,\mathrm{d}V &= \int_{\mathscr{B}} \rho_{\mathrm{f}}\,\mathrm{GRAD}\,\psi \cdot \boldsymbol{K} \cdot \left[\frac{1}{\phi^{\mathrm{f}}\rho_{\mathrm{f}} g}\,\mathrm{GRAD}\left(\frac{\phi^{\mathrm{f}}\theta}{J}\right) + \boldsymbol{F}^{\mathrm{t}} \cdot \frac{\boldsymbol{a} - \mathbf{g}}{g}\right]\mathrm{d}V \\ &= \int_{\mathscr{B}} \rho_{\mathrm{f}}\,\mathrm{grad}\,\psi \cdot \boldsymbol{k} \cdot \left[\frac{1}{\phi^{\mathrm{f}}\rho_{\mathrm{f}} g}\,\mathrm{grad}\left(\frac{\phi^{\mathrm{f}}\theta}{J}\right) + \frac{\boldsymbol{a} - \mathbf{g}}{g}\right]\mathrm{d}V. \end{aligned} \tag{3.16}$$

Expanding (3.24) gives

$$\mathscr{G}_1 + \mathscr{G}_2 + \mathscr{G}_3 + \mathscr{G}_4 = \mathscr{G}_{\mathrm{ext}}(t), \tag{3.17a}$$

$$\mathscr{H}_1 + \mathscr{H}_2 + \mathscr{H}_3 + \mathscr{H}_4 = \mathscr{H}_{\mathrm{ext}}(t), \tag{3.17b}$$

where

$$\begin{aligned} \mathscr{G}_1(\boldsymbol{a}, \boldsymbol{u}, \theta) &= \int_{\mathscr{B}} \rho_0 \boldsymbol{\eta} \cdot \boldsymbol{a}\,\mathrm{d}V, \\ \mathscr{G}_2(\boldsymbol{v}, \boldsymbol{u}) &= \alpha \int_{\mathscr{B}} \mathrm{grad}\,\boldsymbol{\eta} : \mathsf{c} : \mathrm{grad}\,\boldsymbol{v}\,\mathrm{d}V, \\ \mathscr{G}_3(\boldsymbol{u}, \theta) &= \int_{\mathscr{B}} (\mathrm{grad}\,\boldsymbol{\eta} : \boldsymbol{\tau}'_{\mathrm{inv}} - \theta\,\mathrm{div}\,\boldsymbol{\eta})\,\mathrm{d}V, \\ \mathscr{G}_4(\boldsymbol{u}, \theta) &= -\int_{\mathscr{B}} \rho_0 \boldsymbol{\eta} \cdot \mathbf{g}\,\mathrm{d}V, \\ \mathscr{G}_{\mathrm{ext}}(t) &= \int_{\partial\mathscr{B}^t} \boldsymbol{\eta} \cdot \boldsymbol{t}\,\mathrm{d}A \end{aligned} \tag{3.18}$$

and

$$\begin{aligned} \mathscr{H}_1(\boldsymbol{a}, \boldsymbol{u}, \theta) &= -\frac{1}{g} \int_{\mathscr{B}} \rho_{\mathrm{f}}\,\mathrm{grad}\,\psi \cdot \boldsymbol{k} \cdot \boldsymbol{a}\,\mathrm{d}V, \\ \mathscr{H}_2(\boldsymbol{v}, \boldsymbol{u}, \dot{\theta}, \theta) &= \int_{\mathscr{B}} \psi \left(\frac{\rho^{\mathrm{f}}}{K_{\mathrm{f}}}\dot{\theta} + \rho_{\mathrm{f}}\dot{J}\right)\mathrm{d}V, \\ \mathscr{H}_3(\boldsymbol{u}, \theta) &= -\frac{1}{g} \int_{\mathscr{B}} \frac{1}{\phi^{\mathrm{f}}}\,\mathrm{grad}\,\psi \cdot \boldsymbol{k} \cdot \mathrm{grad}\left(\frac{\phi^{\mathrm{f}}\theta}{J}\right)\mathrm{d}V, \\ \mathscr{H}_4(\boldsymbol{u}, \theta) &= \frac{1}{g} \int_{\mathscr{B}} \rho_{\mathrm{f}}\,\mathrm{grad}\,\psi \cdot \boldsymbol{k} \cdot \mathbf{g}\,\mathrm{d}V, \\ \mathscr{H}_{\mathrm{ext}}(t) &= \int_{\partial\mathscr{B}^q} \psi Q\,\mathrm{d}A. \end{aligned} \tag{3.19}$$

Further, $\boldsymbol{u} = \boldsymbol{x} - \boldsymbol{X}$ represents the displacement vector of a material point attached to the solid matrix, so that $\boldsymbol{v} = \dot{\boldsymbol{u}}$ and $\boldsymbol{a} = \ddot{\boldsymbol{u}}$. We note that all $\mathscr{G}_i$’s and $\mathscr{H}_i$’s are functions of the evolving configuration through the displacement vector $\boldsymbol{u}$, as well as of θ whenever the fluid mass density appears inside the integral sign (due to the fluid compressibility). The latter effect is usually ignored in a majority of cases, and if this is done, and the infinitesimal limit is taken, then $\mathscr{G}_4$ and $\mathscr{H}_4$ can be moved to the right-hand side and combined with $\mathscr{G}_{\text{ext}}$ and $\mathscr{H}_{\text{ext}}$, respectively. Finally, we note that damping appears through the term $\mathscr{G}_2$ (viscous damping of the solid matrix) and $\mathscr{H}_2$ (seepage-induced damping).

3.3. Time integration and linearization

We consider the Newmark [54] family of time integration algorithms for the solution of hyperbolic boundary-value problems,

$$\left\{\begin{matrix}\boldsymbol{u}\\ \theta\end{matrix}\right\} = \left\{\begin{matrix}\boldsymbol{u}\\ \theta\end{matrix}\right\}_n + \Delta t\left\{\begin{matrix}\boldsymbol{v}\\ \dot{\theta}\end{matrix}\right\}_n + \frac{\Delta t^2}{2}(1-2\beta)\left\{\begin{matrix}\boldsymbol{a}\\ \ddot{\theta}\end{matrix}\right\}_n + \beta\Delta t^2\left\{\begin{matrix}\boldsymbol{a}\\ \ddot{\theta}\end{matrix}\right\}, \tag{3.20}$$

$$\left\{\begin{matrix}\boldsymbol{v}\\ \dot{\theta}\end{matrix}\right\} = \left\{\begin{matrix}\boldsymbol{v}\\ \dot{\theta}\end{matrix}\right\}_n + (1-\gamma)\Delta t\left\{\begin{matrix}\boldsymbol{a}\\ \ddot{\theta}\end{matrix}\right\}_n + \gamma\Delta t\left\{\begin{matrix}\boldsymbol{a}\\ \ddot{\theta}\end{matrix}\right\}, \tag{3.21}$$

where $\Delta t = t - t_n$ is the time step, the variables with subscripts n are the given starting values associated with time t_n, and β and γ are time integration parameters controlling the accuracy and numerical stability of the algorithm. With fixed starting values at time t_n, the first variations are given by

$$\left\{\begin{matrix}\delta\boldsymbol{u}\\ \delta\theta\end{matrix}\right\} = \beta\Delta t^2\left\{\begin{matrix}\delta\boldsymbol{a}\\ \delta\ddot{\theta}\end{matrix}\right\}, \quad \left\{\begin{matrix}\delta\boldsymbol{v}\\ \delta\dot{\theta}\end{matrix}\right\} = \gamma\Delta t\left\{\begin{matrix}\delta\boldsymbol{a}\\ \delta\ddot{\theta}\end{matrix}\right\}. \tag{3.22}$$

We shall henceforth adopt the acceleration form and express all the variations in terms of $\delta\boldsymbol{a}$ and $\delta\ddot{\theta}$.

The recursion relation takes the form

$$\sum_{i=1}^{4}(\mathscr{G}_i)_{n+1} = \mathscr{G}_{\text{ext}}(t_{n+1}), \quad \sum_{i=1}^{4}(\mathscr{H}_i)_{n+1} = \mathscr{H}_{\text{ext}}(t_{n+1}). \tag{3.23}$$

The right-hand sides are prescribed functions of time, whereas the left hand-sides depend in a nonlinear way on the values of the primary variables as well as on the evolving configurations at each time instant of the solution. Linearized (i.e., tangential, or incremental) versions are sometimes used to solve this system of equations, but here the linearization is aimed at developing an expression for the algorithmic tangent operator useful for Newton iteration. The relevant tangential relations are

$$\sum_{i=1}^{4}\underbrace{\sum_{\square}\frac{\partial\mathscr{G}_i}{\partial(\square)}\delta(\square)}_{\delta\mathscr{G}_i} = \delta\mathscr{G}_{\text{ext}}, \quad \sum_{i=1}^{4}\underbrace{\sum_{\square}\frac{\partial\mathscr{H}_i}{\partial(\square)}\delta(\square)}_{\delta\mathscr{H}_i} = \delta\mathscr{H}_{\text{ext}}, \tag{3.24}$$

where '□' denotes all primary variables on which each of the integral expressions depends. For example, for $\mathscr{G}_1$ the primary variables are $\boldsymbol{a}$, $\boldsymbol{u}$, and θ (see (3.18) and (3.19)). The partial derivatives with respect to '□' have been presented by Borja and Alarcón [25] for most of the integral expressions enumerated above, and below we show the results relevant to dynamic analysis as presented above.

The variation of the Jacobian is

$$\delta J = J\,\text{div}(\delta\boldsymbol{u}) = J\beta\Delta t^2\,\text{div}(\delta\boldsymbol{a}). \tag{3.25}$$

This gives the variations of the volume fractions

$$\delta\phi^{\text{s}} = -\phi^{\text{s}0}J^{-1}\beta\Delta t^2\,\text{div}(\delta\boldsymbol{a}), \quad \delta\phi^{\text{f}} = (1-\phi^{\text{f}0})J^{-1}\beta\Delta t^2\,\text{div}(\delta\boldsymbol{a}), \tag{3.26}$$

where $\phi^{s0} + \phi^{f0} = 1$. We note that $\delta(Jp_f) = \delta\theta = J\delta p_f + p_f\delta J$, and thus the variation of the intrinsic fluid pressure is

$$\delta p_f = \frac{\beta\Delta t^2}{J}[\delta\ddot{\theta} - \theta\,\mathrm{div}(\delta\boldsymbol{a})]. \tag{3.27}$$

From (3.8), the variation of the intrinsic fluid mass density is

$$\delta\rho_f = \frac{\rho_f}{K_f}\delta p_f = \frac{\rho_f\beta\Delta t^2}{K_f J}[\delta\ddot{\theta} - \theta\,\mathrm{div}(\delta\boldsymbol{a})], \tag{3.28}$$

and so the variation of the total mass density (with $\delta\rho_s = 0$ from the assumed incompressibility of the solid grains) is

$$\delta\rho = \rho_s\delta\phi^s + \rho_f\delta\phi^f + \phi^f\delta\rho_f = \beta\Delta t^2[c_1\delta\ddot{\theta} + c_3\,\mathrm{div}(\delta\boldsymbol{a})], \tag{3.29}$$

where

$$c_1 = \frac{\phi^f\rho_f}{K_f J}, \quad c_2 = \frac{1}{J}\left[\rho_f(1-\phi^{f0}) - \phi^f\rho_f\frac{\theta}{K_f}\right], \quad c_3 = c_2 - \rho_s\phi^{s0}/J. \tag{3.30}$$

Thus, the variation of the pull-back total mass density ρ_0 is

$$\delta\rho_0 = \delta(J\rho) = J\delta\rho + \rho\delta J = J\beta\Delta t^2[c_1\delta\ddot{\theta} + (c_3+\rho)\,\mathrm{div}(\delta\boldsymbol{a})]. \tag{3.31}$$

As noted earlier, $\delta\rho_0 \neq 0$ since the mass of the fluid phase is not conserved by the motion of the solid phase.

The variation of $\mathscr{G}_1$ from the chain rule is

$$\begin{aligned}\delta\mathscr{G}_1 &= \int_{\mathscr{B}}\rho_0\boldsymbol{\eta}\cdot\delta\boldsymbol{a}\,\mathrm{d}V + \int_{\mathscr{B}}\delta\rho_0\boldsymbol{\eta}\cdot\boldsymbol{a}\,\mathrm{d}V \\ &= \int_{\mathscr{B}}\rho_0\boldsymbol{\eta}\cdot\delta\boldsymbol{a}\,\mathrm{d}V + \beta\Delta t^2\int_{\mathscr{B}}Jc_1\boldsymbol{\eta}\cdot\boldsymbol{a}\delta\ddot{\theta}\,\mathrm{d}V + \beta\Delta t^2\int_{\mathscr{B}}(Jc_3+\rho_0)\boldsymbol{\eta}\cdot\boldsymbol{a}\,\mathrm{div}(\delta\boldsymbol{a})\,\mathrm{d}V.\end{aligned} \tag{3.32}$$

With $\delta\boldsymbol{F} = \mathrm{grad}(\delta\boldsymbol{u})\cdot\boldsymbol{F}$, $\delta\boldsymbol{F}^{-1} = -\boldsymbol{F}^{-1}\cdot\mathrm{grad}(\delta\boldsymbol{u})$, and $\delta(\mathrm{grad}\,\boldsymbol{\psi}) = \mathrm{grad}\,\delta\boldsymbol{\psi} - \mathrm{grad}\,\boldsymbol{\psi}\cdot\mathrm{grad}(\delta\boldsymbol{u})$, we have

$$\delta\mathscr{G}_2 = \alpha\int_{\mathscr{B}}\delta(\mathrm{grad}\,\boldsymbol{\eta}):\mathsf{c}:\mathrm{grad}\,\boldsymbol{v}\,\mathrm{d}V + \alpha\int_{\mathscr{B}}\mathrm{grad}\,\boldsymbol{\eta}:\delta\mathsf{c}:\mathrm{grad}\,\boldsymbol{v}\,\mathrm{d}V + \alpha\int_{\mathscr{B}}\mathrm{grad}\,\boldsymbol{\eta}:\mathsf{c}:\delta(\mathrm{grad}\,\boldsymbol{v})\,\mathrm{d}V, \tag{3.33}$$

where

$$\begin{aligned}&\delta(\mathrm{grad}\,\boldsymbol{\eta}) = -\beta\Delta t^2\,\mathrm{grad}\,\boldsymbol{\eta}\cdot\mathrm{grad}(\delta\boldsymbol{a}),\\ &\delta(\mathrm{grad}\,\boldsymbol{v}) = \gamma\Delta t\,\mathrm{grad}(\delta\boldsymbol{a}) - \beta\Delta t^2\,\mathrm{grad}\,\boldsymbol{v}\cdot\mathrm{grad}(\delta\boldsymbol{a}),\\ &\delta\mathsf{c} = 2(\delta\mu')\boldsymbol{I} = -\lambda\beta\Delta t^2\,\mathrm{div}(\delta\boldsymbol{a})\boldsymbol{I}.\end{aligned} \tag{3.34}$$

We note that $\delta\boldsymbol{\eta} \equiv \boldsymbol{0}$ since $\boldsymbol{\eta}$ is a weighting function.

The variation of $\mathscr{G}_3$ has been presented in [25], and here we simply show the result

$$\delta\mathscr{G}_3 = \beta\Delta t^2\int_{\mathscr{B}}\mathrm{grad}\,\boldsymbol{\eta}:(\mathsf{c}+\boldsymbol{\tau}'_{\mathrm{inv}}\oplus\boldsymbol{1}):\mathrm{grad}(\delta\boldsymbol{a})\,\mathrm{d}V - \beta\Delta t^2\int_{\mathscr{B}}[(\delta\ddot{\theta})\mathrm{div}\,\boldsymbol{\eta} - \theta\,\mathrm{grad}^{\mathrm{t}}\boldsymbol{\eta}:\mathrm{grad}(\delta\boldsymbol{a})]\,\mathrm{d}V, \tag{3.35}$$

where $(\boldsymbol{\tau}'_{\mathrm{inv}}\oplus\boldsymbol{1})_{ijkl} = (\tau'_{\mathrm{inv}})_{jl}\delta_{ik}$ is the stress contribution to the moduli. Also,

$$\delta\mathscr{G}_4 = -\int_{\mathscr{B}}\delta\rho_0\boldsymbol{\eta}\cdot\mathbf{g}\,\mathrm{d}V = -\beta\Delta t^2\int_{\mathscr{B}}J[c_1\delta\ddot{\theta} + (c_3+\rho)\mathrm{div}(\delta\boldsymbol{a})]\boldsymbol{\eta}\cdot\mathbf{g}\,\mathrm{d}V \tag{3.36}$$

and

$$\delta\mathscr{G}_{\text{ext}} = \int_{\mathscr{B}^t} \boldsymbol{\eta} \cdot \delta\boldsymbol{t}\,\mathrm{d}A \tag{3.37}$$

for the case of dead loading.

Next, we obtain the variation of $\mathscr{H}_1$, assuming $\boldsymbol{k}$ =constant, as

$$\delta\mathscr{H}_1 = -\frac{1}{g}\int_{\mathscr{B}} \rho_{\mathrm{f}}\,\mathrm{grad}\,\psi \cdot \boldsymbol{k} \cdot \delta\boldsymbol{a}\,\mathrm{d}V - \frac{1}{g}\int_{\mathscr{B}} \rho_{\mathrm{f}}\delta(\mathrm{grad}\,\psi) \cdot \boldsymbol{k} \cdot \boldsymbol{a}\,\mathrm{d}V - \frac{1}{g}\int_{\mathscr{B}} \delta\rho_{\mathrm{f}}\,\mathrm{grad}\,\psi \cdot \boldsymbol{k} \cdot \boldsymbol{a}\,\mathrm{d}V. \tag{3.38}$$

Alternative forms for the second and third integrals on the right-hand side are given below,

$$\int_{\mathscr{B}} \rho_{\mathrm{f}}\delta(\mathrm{grad}\,\psi) \cdot \boldsymbol{k} \cdot \boldsymbol{a}\,\mathrm{d}V = -\beta\Delta t^2 \int_{\mathscr{B}} \rho_{\mathrm{f}}[\mathrm{grad}\,\psi \otimes (\boldsymbol{k} \cdot \boldsymbol{a})] : \mathrm{grad}(\delta\boldsymbol{a})\mathrm{d}V \tag{3.39}$$

and

$$\int_{\mathscr{B}} \delta\rho_{\mathrm{f}}\,\mathrm{grad}\,\psi \cdot \boldsymbol{k} \cdot \boldsymbol{a}\,\mathrm{d}V = \frac{\beta\Delta t^2}{K_{\mathrm{f}}} \int_{\mathscr{B}} \frac{\rho_{\mathrm{f}}}{J}\,\mathrm{grad}\,\psi \cdot \boldsymbol{k} \cdot \boldsymbol{a}[\delta\ddot{\theta} - \theta\,\mathrm{div}(\delta\boldsymbol{a})]\mathrm{d}V. \tag{3.40}$$

The variation of $\mathscr{H}_2$ is

$$\delta\mathscr{H}_2 = \frac{1}{K_{\mathrm{f}}}\int_{\mathscr{B}} \psi(\rho^{\mathrm{f}}\delta\dot{\theta} + \dot{\theta}\delta\rho^{\mathrm{f}})\,\mathrm{d}V + \int_{\mathscr{B}} \psi(\rho_{\mathrm{f}}\delta\dot{J} + \delta\rho_{\mathrm{f}}\dot{J})\,\mathrm{d}V. \tag{3.41}$$

Since $\delta\rho^{\mathrm{f}} = \phi^{\mathrm{f}}\delta\rho_{\mathrm{f}} + \delta\phi^{\mathrm{f}}\rho_{\mathrm{f}} = \beta\Delta t^2[c_1\delta\ddot{\theta} + c_2\,\mathrm{div}(\delta\boldsymbol{a})]$ from (3.30), an alternative form for the first integral on the right-hand side of (3.41) is

$$\frac{1}{K_{\mathrm{f}}}\int_{\mathscr{B}} \psi(\rho^{\mathrm{f}}\delta\dot{\theta} + \dot{\theta}\delta\rho^{\mathrm{f}})\mathrm{d}V = \frac{\gamma\Delta t}{K_{\mathrm{f}}}\int_{\mathscr{B}} \psi\rho^{\mathrm{f}}\delta\ddot{\theta}\,\mathrm{d}V + \frac{\beta\Delta t^2}{K_{\mathrm{f}}}\int_{\mathscr{B}} \psi\dot{\theta}[c_1\delta\ddot{\theta} + c_2\,\mathrm{div}(\delta\boldsymbol{a})]\,\mathrm{d}V. \tag{3.42}$$

We recall the relation (see [25])

$$\delta\dot{J} = J[\mathrm{div}(\delta\boldsymbol{v}) - \mathrm{grad}^{\mathrm{t}}\boldsymbol{v} : \mathrm{grad}(\delta\boldsymbol{u}) + \mathrm{div}\,\boldsymbol{v}\,\mathrm{div}(\delta\boldsymbol{u})]. \tag{3.43}$$

We can thus rewrite the second integral on the right-hand side of (3.41) as

$$\begin{aligned}\int_{\mathscr{B}} \psi(\rho_{\mathrm{f}}\delta\dot{J} + \delta\rho_{\mathrm{f}}\dot{J})\mathrm{d}V = {}& \gamma\Delta t\int_{\mathscr{B}} \psi J\rho_{\mathrm{f}}\,\mathrm{div}(\delta\boldsymbol{a})\mathrm{d}V + \frac{\beta\Delta t^2}{K_{\mathrm{f}}}\int_{\mathscr{B}} \psi\rho_{\mathrm{f}}\,\mathrm{div}\,\boldsymbol{v}\delta\ddot{\theta}\mathrm{d}V \\ & + \beta\Delta t^2\int_{\mathscr{B}} \psi\rho_{\mathrm{f}}\left[\left(J - \frac{\theta}{K_{\mathrm{f}}}\right)\mathrm{div}\,\boldsymbol{v}\,\mathrm{div}(\delta\boldsymbol{a}) - J\,\mathrm{grad}^{\mathrm{t}}\boldsymbol{v} : \mathrm{grad}(\delta\boldsymbol{a})\right]\mathrm{d}V.\end{aligned} \tag{3.44}$$

The variation of $\mathscr{H}_3$ is

$$\begin{aligned}\delta\mathscr{H}_3 = {}& -\frac{1}{g}\int_{\mathscr{B}} \delta\left(\frac{1}{\rho_{\mathrm{f}}}\right)\mathrm{grad}\,\psi \cdot \boldsymbol{k} \cdot \mathrm{grad}\left(\frac{\phi^{\mathrm{f}}\theta}{J}\right)\mathrm{d}V \\ & -\frac{1}{g}\int_{\mathscr{B}} \frac{1}{\rho_{\mathrm{f}}}\delta(\mathrm{grad}\,\psi) \cdot \boldsymbol{k} \cdot \mathrm{grad}\left(\frac{\phi^{\mathrm{f}}\theta}{J}\right)\mathrm{d}V \\ & -\frac{1}{g}\int_{\mathscr{B}} \frac{1}{\rho_{\mathrm{f}}}\,\mathrm{grad}\,\psi \cdot \boldsymbol{k} \cdot \delta\left[\mathrm{grad}\left(\frac{\phi^{\mathrm{f}}\theta}{J}\right)\right]\mathrm{d}V,\end{aligned} \tag{3.45}$$

where

$$\begin{aligned}
&\delta\left(\frac{1}{\rho_{\mathrm{f}}}\right)=\frac{\beta\Delta t^2}{K_{\mathrm{f}}J}[\theta\,\mathrm{div}(\delta\boldsymbol{a})-\delta\ddot{\theta}],\\
&\delta(\mathrm{grad}\,\psi)=-\beta\Delta t^2\,\mathrm{grad}\,\psi\cdot\mathrm{grad}(\delta\boldsymbol{a}),\\
&\delta\left[\mathrm{grad}\left(\frac{\phi^{\mathrm{f}}\theta}{J}\right)\right]=\beta\Delta t^2\,\mathrm{grad}\left[\left(\frac{\phi_{\mathrm{f}}}{J}\right)\delta\ddot{\theta}+\theta\left(\frac{\phi^{\mathrm{s0}}}{J^2}-\frac{\phi^{\mathrm{f}}}{J}\right)\mathrm{div}(\delta\boldsymbol{a})\right]-\beta\Delta t^2\,\mathrm{grad}\left(\frac{\phi^{\mathrm{f}}\theta}{J}\right)\cdot\mathrm{grad}(\delta\boldsymbol{a}).
\end{aligned} \tag{3.46}$$

Note again that the variation of the weighting function ψ is zero.

Finally, we obtain the variation of $\mathscr{H}_4$ as

$$\delta\mathscr{H}_4=\frac{1}{g}\int_{\mathscr{B}}\delta\rho_{\mathrm{f}}\,\mathrm{grad}\,\psi\cdot\boldsymbol{k}\cdot\mathbf{g}\,\mathrm{d}V+\frac{1}{g}\int_{\mathscr{B}}\rho_{\mathrm{f}}\delta(\mathrm{grad}\,\psi)\cdot\boldsymbol{k}\cdot\mathbf{g}\,\mathrm{d}V, \tag{3.47}$$

Alternative forms for the integrals are given below,

$$\int_{\mathscr{B}}\delta\rho_{\mathrm{f}}\,\mathrm{grad}\,\psi\cdot\boldsymbol{k}\cdot\mathbf{g}\,\mathrm{d}V=\frac{\beta\Delta t^2}{K_{\mathrm{f}}}\int_{\mathscr{B}}\frac{\rho_{\mathrm{f}}}{J}\,\mathrm{grad}\,\psi\cdot\boldsymbol{k}\cdot\mathbf{g}[\delta\ddot{\theta}-\theta\,\mathrm{div}(\delta\boldsymbol{a})]\mathrm{d}V \tag{3.48}$$

and

$$\int_{\mathscr{B}}\rho_{\mathrm{f}}\delta(\mathrm{grad}\,\psi)\cdot\boldsymbol{k}\cdot\mathbf{g}\,\mathrm{d}V=-\beta\Delta t^2\int_{\mathscr{B}}\rho_{\mathrm{f}}[\mathrm{grad}\,\psi\otimes(\boldsymbol{k}\cdot\mathbf{g})]:\mathrm{grad}(\delta\boldsymbol{a})\mathrm{d}V. \tag{3.49}$$

Also,

$$\delta\mathscr{H}_{\mathrm{ext}}=\int_{\mathscr{B}^q}\psi\delta Q\,\mathrm{d}A. \tag{3.50}$$

To summarize, all the variations of the configuration-dependent integrals are expressible in terms of the acceleration fields $\delta\boldsymbol{a}$ and $\delta\ddot{\theta}$.

3.4. Matrix equations and mixed finite elements

Using the standard Galerkin approximation, we construct shape functions and interpolate the solid matrix displacements and fluid pressure functions through their nodal values. Let $\boldsymbol{d}$, $\dot{\boldsymbol{d}}$, and $\ddot{\boldsymbol{d}}$ be the nodal values of the solid displacement, velocity, and acceleration fields, respectively; and $\boldsymbol{\theta}$, $\dot{\boldsymbol{\theta}}$, and $\ddot{\boldsymbol{\theta}}$ the nodal values of the fluid pressure function and their first and second time derivatives, respectively. The matrix equations for balance of momentum and balance of mass take the form

$$\boldsymbol{M}_1\ddot{\boldsymbol{d}}+\boldsymbol{C}_1\dot{\boldsymbol{d}}+\boldsymbol{N}_1(\boldsymbol{d},\boldsymbol{\theta})-\boldsymbol{G}_{\mathrm{ext}}=\boldsymbol{0}, \tag{3.51}$$

$$\boldsymbol{M}_2\ddot{\boldsymbol{d}}+\boldsymbol{C}_2\dot{\boldsymbol{d}}+\boldsymbol{C}_3\dot{\boldsymbol{\theta}}+\boldsymbol{N}_2(\boldsymbol{d},\boldsymbol{\theta})-\boldsymbol{H}_{\mathrm{ext}}=\boldsymbol{0}. \tag{3.52}$$

All of the coefficient matrices and vectors have standard forms, and below we simply summarize the sources of each term in the matrix equations, see (3.18) and (3.19)

$$\begin{aligned}
&\boldsymbol{M}_1\ddot{\boldsymbol{d}}\leftarrow\mathscr{G}_1,\quad \boldsymbol{C}_1\dot{\boldsymbol{d}}\leftarrow\mathscr{G}_2,\quad \boldsymbol{N}_1(\boldsymbol{d},\boldsymbol{\theta})\leftarrow\mathscr{G}_3,\quad \boldsymbol{G}_{\mathrm{ext}}\leftarrow\mathscr{G}_4,\mathscr{G}_{\mathrm{ext}};\quad \boldsymbol{M}_2\ddot{\boldsymbol{d}}\leftarrow\mathscr{H}_1,\\
&\boldsymbol{C}_2\dot{\boldsymbol{d}}+\boldsymbol{C}_3\dot{\boldsymbol{\theta}}\leftarrow\mathscr{H}_2,\quad \boldsymbol{N}_2(\boldsymbol{d},\boldsymbol{\theta})\leftarrow\mathscr{H}_3,\quad \boldsymbol{H}_{\mathrm{ext}}\leftarrow\mathscr{H}_4,\mathscr{H}_{\mathrm{ext}}.
\end{aligned} \tag{3.53}$$

Nonlinearities arise from the fact that all matrices and vectors are configuration-dependent, including some of the terms in the external force vectors $\boldsymbol{G}_{\mathrm{ext}}$ and $\boldsymbol{H}_{\mathrm{ext}}$. In addition, the material model itself is nonlinear hyperelastic, which also contributes to the nonlinearity.

The two matrix equations may be combined to yield the composite system

$$\begin{bmatrix} \boldsymbol{M}_1 & \mathbf{0} \\ \boldsymbol{M}_2 & \mathbf{0} \end{bmatrix} \begin{Bmatrix} \ddot{\boldsymbol{d}} \\ \ddot{\boldsymbol{\theta}} \end{Bmatrix} + \begin{bmatrix} \boldsymbol{C}_1 & \mathbf{0} \\ \boldsymbol{C}_2 & \boldsymbol{C}_3 \end{bmatrix} \begin{Bmatrix} \dot{\boldsymbol{d}} \\ \dot{\boldsymbol{\theta}} \end{Bmatrix} + \begin{Bmatrix} \boldsymbol{N}_1 \\ \boldsymbol{N}_2 \end{Bmatrix} - \begin{Bmatrix} \boldsymbol{G}_{\text{ext}} \\ \boldsymbol{H}_{\text{ext}} \end{Bmatrix} = \begin{Bmatrix} \mathbf{0} \\ \mathbf{0} \end{Bmatrix}. \tag{3.54}$$

As in the variational formulation, Newmark's method can once again be used to integrate this system

$$\begin{Bmatrix} \boldsymbol{d} \\ \boldsymbol{\theta} \end{Bmatrix} = \begin{Bmatrix} \boldsymbol{d} \\ \boldsymbol{\theta} \end{Bmatrix}_n + \Delta t \begin{Bmatrix} \dot{\boldsymbol{d}} \\ \dot{\boldsymbol{\theta}} \end{Bmatrix}_n + \frac{\Delta t^2}{2}(1-2\beta) \begin{Bmatrix} \ddot{\boldsymbol{d}} \\ \ddot{\boldsymbol{\theta}} \end{Bmatrix}_n + \beta \Delta t^2 \begin{Bmatrix} \ddot{\boldsymbol{d}} \\ \ddot{\boldsymbol{\theta}} \end{Bmatrix}, \tag{3.55}$$

$$\begin{Bmatrix} \dot{\boldsymbol{d}} \\ \dot{\boldsymbol{\theta}} \end{Bmatrix} = \begin{Bmatrix} \dot{\boldsymbol{d}} \\ \dot{\boldsymbol{\theta}} \end{Bmatrix}_n + (1-\gamma)\Delta t \begin{Bmatrix} \ddot{\boldsymbol{d}} \\ \ddot{\boldsymbol{\theta}} \end{Bmatrix}_n + \gamma \Delta t \begin{Bmatrix} \ddot{\boldsymbol{d}} \\ \ddot{\boldsymbol{\theta}} \end{Bmatrix}, \tag{3.56}$$

where β and γ are integration parameters, and Δt is the time step. Note in (3.54) that $\ddot{\boldsymbol{\theta}}$ does not enter into the equilibrium equation; however, Newmark's method still requires this variable to calculate $\boldsymbol{\theta}$ and $\dot{\boldsymbol{\theta}}$. Substituting into (3.54) thus leads to a system of nonlinear matrix equations in the unknown nodal acceleration vectors $\ddot{\boldsymbol{d}}$ and $\ddot{\boldsymbol{\theta}}$, which can be solved by Newton's method.

Linearized forms of the matrix equations are needed to solve the system of equations described above. An exact tangent operator is available in closed form, as already illustrated in the preceding section. It must be noted, however, that some terms in the tangent operator are not easily amenable to coding. Fortunately, most of these terms result in numerically small values and contribute very little to enhance the convergence of the iteration, and thus are simply dropped out. Note that the tangent operator is used only for iteration purposes, and provided the iteration has sufficiently converged no additional approximation is engendered by ignoring some of its terms.

For the record, the terms ignored in the tangent operator pertain to those of $\mathscr{G}_2$, specifically all the terms involving $\mathrm{O}(\Delta t^2)$. Thus

$$\delta\mathscr{G}_2 \approx \alpha\gamma\Delta t \int_{\mathscr{B}} \operatorname{grad}\boldsymbol{\eta} : \mathsf{c} : \operatorname{grad}(\delta\boldsymbol{a})\,\mathrm{d}V.$$

Due to the high value of the fluid bulk modulus K_{f}, it may also be possible to ignore all the terms having this quantity in the denominator, but in the present work we decided to keep them in the formulation. All integrals are evaluated by numerical integration, and 'mixed' terms such as $\operatorname{grad}(\phi^{\mathrm{f}}\theta/J)$ in the expression

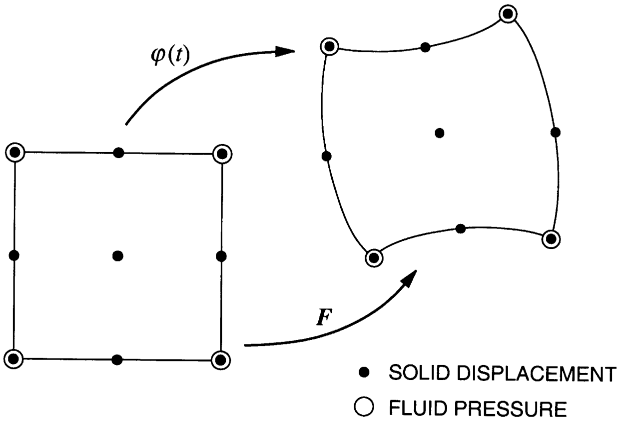

Fig. 2. Motion of solid displacement and fluid pressure nodes in a Q9P4 mixed finite element. Pressure nodes attached to the solid matrix translate to a new configuration along with displacement nodes.

for $\mathscr{H}_3$ are evaluated at the integration points by interpolating from the nodal values of θ and combining with the values of ϕ^{f} and J at the quadrature points.

As for the time integration, we noted earlier that all material time derivatives are developed following the motion of the solid matrix, allowing standard mixed finite element interpolations with displacement and fluid pressure nodes to be employed. Fig. 2 shows the motion of a Q9P4 plane strain mixed finite element, with a nine-node biquadratic Lagrangian interpolation for the displacement field and a four-node bilinear interpolation for the fluid pressure. The time variation of the pressure function is reckoned with respect to the moving solid matrix, and hence the pore pressure node may be attached to the solid matrix and move along with the displacement node. This particular element is commonly used for 'mixed' finite element analysis in the infinitesimal regime, and passes the LBB condition for infinitesimal deformation [58].

4. Numerical simulations

In this section we present one- and two-dimensional (plane strain) examples highlighting the difference between the small and finite deformation analyses of fully saturated porous media. Two finite element codes are used for this purpose: one based on the infinitesimal formulation in which the geometric effects are completely ignored, and a second based on the proposed finite deformation theory. Details of the infinitesimal model are given by Li and Borja [59]. Both the infinitesimal and finite deformation codes utilize the Q9P4 mixed finite elements for the spatial interpolation of the solid displacement and fluid pressure fields, as well as the Newmark time integration scheme, with time integration parameters $\beta = 0.3025$ and $\gamma = 0.6$. Note that for the linear theory, $2\beta \geqslant \gamma \geqslant 1/2$ results in an unconditionally stable algorithm [58]. Also, in the infinitesimal regime the neo-Hookean hyperelastic solid readily degenerates to the conventional Hookean material of linear elasticity, thus making the comparison between the infinitesimal and finite deformation solutions meaningful.

4.1. Porous layer under uniform step load

As a first example we consider a porous layer of initial thickness $H_0 = 10$ m subjected to a uniform step load. Although this problem is one-dimensional, we model it as a plane strain problem consisting of a saturated solid matrix column 10 m deep, see Fig. 3. The upper boundary is perfectly drained and subjected to a step load of intensity w; the remaining boundaries are rigid and impervious. The assumed material parameters are: Lamé constants for the solid matrix (in MPa) $\lambda = 29$ and $\mu = 7$; initial volume fractions $\phi^{\mathrm{s}0} = 0.58$ and $\phi^{\mathrm{f}0} = 0.42$; reference intrinsic mass densities (in kg/m^3) $\rho_{\mathrm{s}0} = 2700$ and $\rho_{\mathrm{f}0} = 1000$; fluid bulk stiffness $K_{\mathrm{f}} = 2.2 \times 10^4$ MPa; hydraulic conductivity $\boldsymbol{k} = \kappa\mathbf{1}$ (isotropic), where $\kappa = 0.1$ m/s; and solid matrix damping coefficient $\alpha = 0$ (inviscid hyperelastic response). The time step was taken as $\Delta t = 0.01$ s; other time steps were also tested but they appear to have no significant influence on the response histories reported herein. The very high fluid bulk modulus, typical for water [57], makes the fluid phase much more incompressible compared to the solid matrix.

The analytical solution for the steady-state compression ΔH in the geometrically linear regime is

$$\Delta H = \frac{wH_0}{M_{\mathrm{c}}}, \quad M_{\mathrm{c}} = \lambda + 2\mu, \tag{4.1}$$

where M_{c} is the constrained modulus of the solid matrix. For a surface load $w = 40$ kPa, Fig. 4 shows the time variations of the predicted compression by the small and finite deformation analyses, along with the steady-state analytical solution. Because the compression of the porous layer is so small, both numerical models predict essentially the same compression-time responses, including the steady-state responses which agree with the analytical solution. On the other hand, with higher loads, $w = 2$, 4, and 8 MPa, Fig. 5 shows

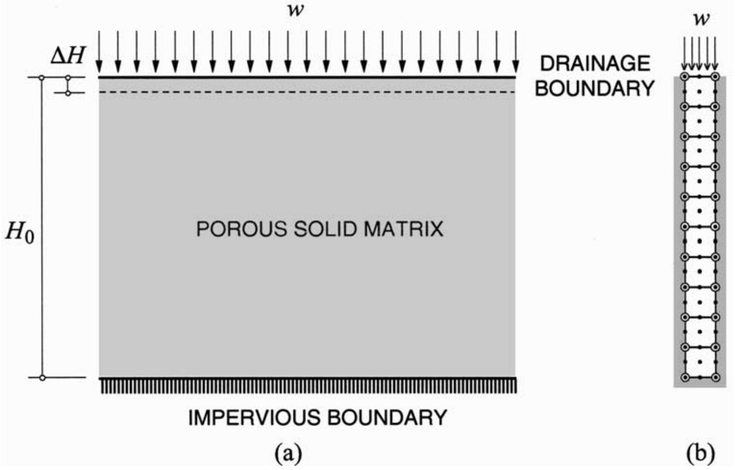

Fig. 3. Porous layer under uniform step load: (a) problem geometry; (b) finite element mesh.

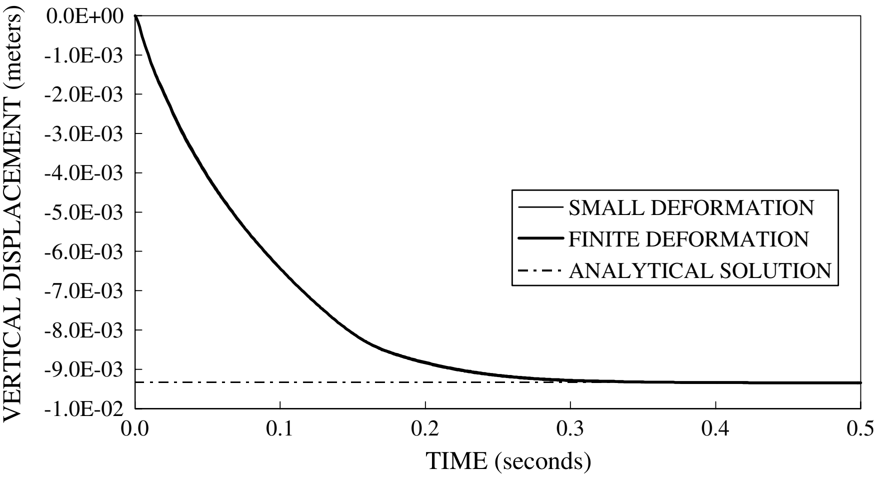

Fig. 4. Porous layer under uniform strip load: vertical displacement–time histories at a load level $w(t) = 40$ kPa.

the small deformation solutions consistenly predicting larger vertical compression compared to the corresponding finite deformation solutions.

4.2. Porous matrix under partial compression

As a second example, we consider a porous matrix under partial compression and deforming in plane strain. The finite element mesh for this problem is shown in Fig. 6. The mesh is composed of 100 Q9P4 mixed elements of dimensions 1 m × 1 m. The loaded part of the top surface is an impervious boundary; the free part is a drainage boundary. The right and left vertical boundaries are supported horizontally by rollers, and impervious; the bottom surface is supported vertically by rollers and is also impervious. The assumed material parameters are as follows: Lamé constants (in MPa) $\lambda = 8.4$ and $\mu = 5.6$; initial volume

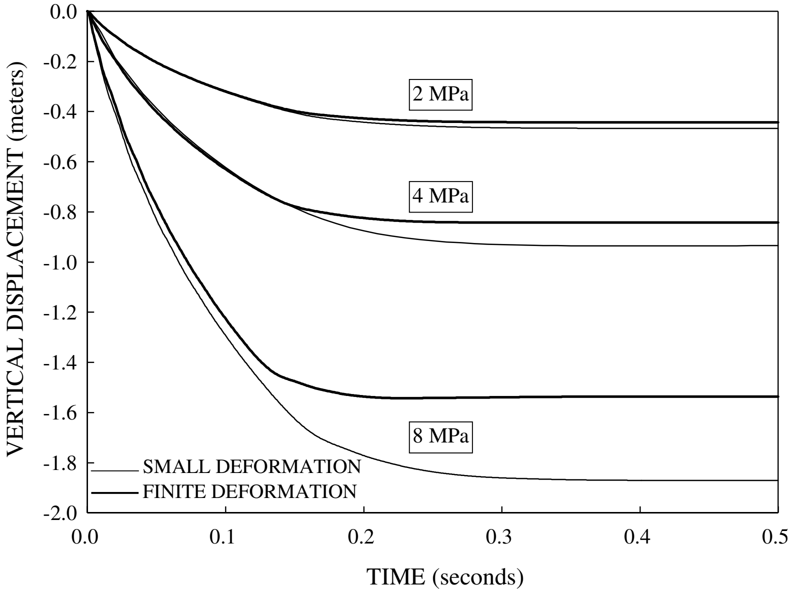

Fig. 5. Porous layer under uniform strip load: vertical displacement–time histories at load levels $w(t) = 2$, 4 and 8 MPa.

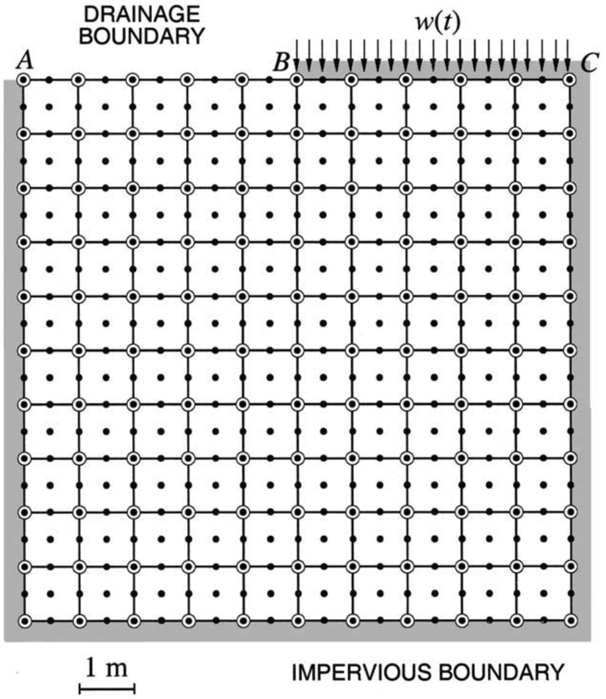

Fig. 6. Porous matrix under partial compression. Surface pressure $w(t)$ is a step load; vertical sides and bottom boundary are impervious and on roller supports, upper side AB is a drainage boundary, while upper side BC is an impervious boundary.

fractions $\phi^{s0} = 0.58$ and $\phi^{f0} = 0.42$; reference intrinsic mass densities (in kg/m^3) $\rho_{s0} = 2700$ and $\rho_{f0} = 1000$; fluid bulk stiffness $K_f = 2.2 \times 10^4$ MPa; hydraulic conductivity $\boldsymbol{k} = \kappa\mathbf{1}$ (isotropic), where $\kappa = 1.0 \times 10^{-4}$ m/s; and solid matrix damping coefficient $\alpha = 0$ (inviscid hyperelastic response).

The choice of an 'optimal' time step Δt for a given finite element discretization is an important aspect of dynamic analysis. It is well known that simply reducing the time step while holding the mesh length fixed in fact worsens the results since in this case we converge to the exact solution of the spatially discrete, temporally continuous system rather than the exact solution of the original partial differential equations [58]. Obviously, the accuracy of the solution also worsens when the time step is very large. For these reasons, it is desirable to compute at a time step as close to critical as possible, and for a three-node (quadratic) rod element the critical time step is [58]

$$\Delta t = \frac{h}{\sqrt{6}c}, \tag{4.2}$$

where h is the element length and c is the characteristic wave speed.

In a porous medium three types of body waves exist: a shear wave, a longitudinal wave of the first kind, and a longitudinal wave of the second kind [44,45,60]. The speed of the shear wave in an elastic porous medium is given by Coussy [48] as

$$c_s = \left(\frac{\mu}{\rho^s + \xi\rho^f}\right)^{1/2}, \tag{4.3}$$

where μ is the elastic shear modulus (also equal to the Lamé constant μ) and ξ is a function of the tortuosity of flow. If we set $\xi = 1$, then the denominator in (4.3) becomes equal to the saturated mass density ρ and we recover the wave speed under a fully undrained condition. For the problem at hand, $\rho^{s0} + \rho^{f0} = 2000$ kg/m^3, and $c_s \approx 53$ m/s. The longitudinal wave speeds are not as straightforward to estimate since they generally depend on the elastic and dynamic properties of the material, including its hydraulic conductivity [44,45,48].

An alternative approach to estimating the speed of the most significant wave (and thus, get an idea of the critical time step to use in the numerical simulations) is to perform a preliminary analysis. Here we apply a surface load $w(t) = 15$ kPa on the mesh of Fig. 6 and plot the temporal variations of the vertical displacements of corner nodes A and C in Fig. 7, using a trial time step of $\Delta t = 0.01$ s. The applied load in this case is so small that the small deformation and finite deformation analyses resulted in nearly identical response histories. Fig. 7 shows that nodes A and C move by almost the same amount but in opposite directions, suggesting a nearly undrained (or nearly incompressible) deformation response of the porous structure. Also, we see that the step load produces a disturbance which is reflected back after a time period of approximately 0.5 s. If we consider this disturbance to have traveled over a distance equal to twice the mesh dimensions (20 m in this case), then the speed of the significant wave is roughly 40 m/s, which is nearly equal to the previously estimated shear wave velocity. Note that the hydraulic conductivity for this example is so small that the solution at $t = 2$ s should not be construed as corresponding to end of consolidation.

To investigate the influence of the hydraulic conductivity on the speed of the significant wave, we repeat the analysis but this time assume a much higher value of hydraulic conductivity, $\kappa = 0.1$ m/s. Fig. 8 shows the time histories of the vertical displacements of corner nodes A and C. We see that corner node A approaches a steady-state vertical downward displacement of 0.5 mm whereas node C approaches a downward displacement of 8 mm, suggesting a significant compaction of the porous matrix in the vicinity of the surface load w due to significant drainage that took place over the course of the solution. Note, however, that the time interval between successive reflected waves remains nearly equal to 0.5 s, suggesting that the wave speed is not significantly affected by the value of the hydraulic conductivity.

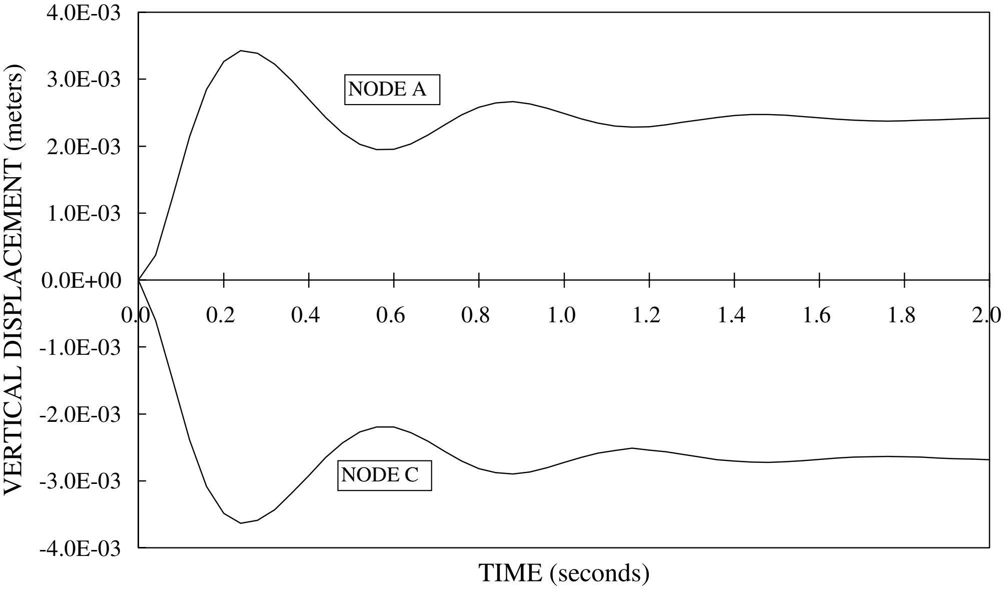

Fig. 7. Porous matrix under partial compression: vertical displacement–time histories of corner nodes A and C at hydraulic conductivity $\kappa = 0.0001$ m/s.

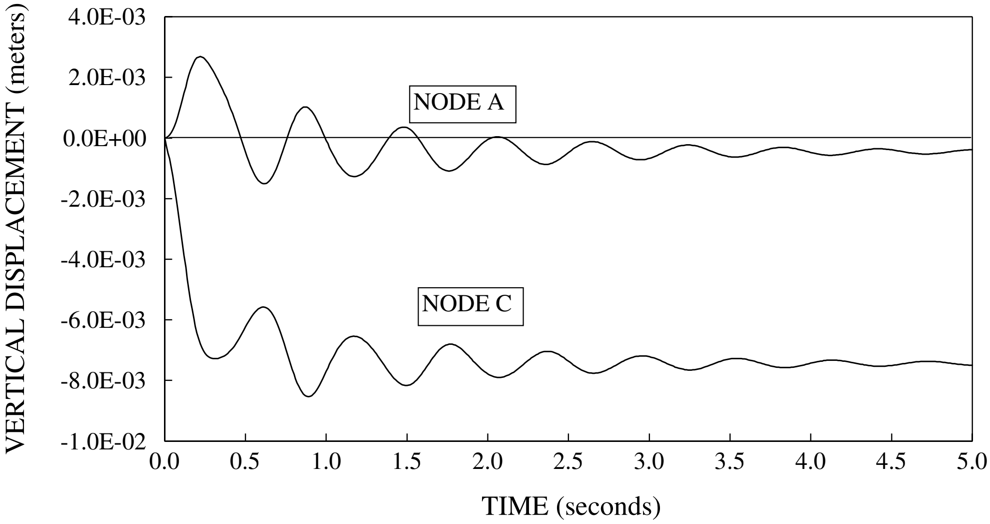

Fig. 8. Porous matrix under partial compression: vertical displacement–time histories of corner nodes A and C at hydraulic conductivity $\kappa = 0.1$ m/s.

If we set the wave speed at $c = 40$ m/s and the element dimension at 1 m, then (4.2) gives a critical time step of $\Delta t = 0.0102$ s. It is thus desirable to select a time step that is very close to this value, and in the remaining analyses we assume a time step of $\Delta t = 0.01$ s. It must be noted that the time interval between successive waves is not affected much by the time step, i.e., we did not obtain a wave speed of

40 m/s because we utilized a trial time step of 0.01 s in the preliminary analysis; if we had used a different time step we would have obtained approximately the same wave speed, although the response histories would have different amplitudes (and even shapes). This latter statement is elaborated further below.

With these preliminary results at hand, we now proceed with the finite deformation simulations and apply a much higher step load $w(t) = 3$ MPa (with the hydraulic conductivity remaining at a value $\kappa = 0.1$ m/s). The objectives of the remaining part of the analysis are to compare the small and finite deformation solutions and investigate the effect of the solid matrix damping coefficient α on the predicted response history curves. To this end, we perform small and finite deformation numerical calculations at the following values of damping coefficient α: 0.002, 0.02, and 0.2 s. Figs. 9 and 10 show the resulting vertical displacement response histories for nodes A (upper left corner), B (upper middle node), and C (upper right corner) of the mesh.

Figs. 9 and 10 show that the greatest oscillations occur at the corner nodes, and the least oscillation at the middle node, which is to be expected. The time interval between successive waves remains approximately equal to 0.5 s, suggesting the wave speed is not greatly influenced by the value of the damping coefficient and the nature of analysis (small deformation or finite deformation). Oscillations at the corner nodes persist over a long period of time with a small α, but the steady-state solution is achieved over a short period of time with a large α. This indicates a more significant effect of the solid matrix damping as compared to the seepage-induced damping (since the latter type of damping is present in all the solutions anyway). Finally, the finite deformation solutions consistently predict smaller vertical displacements compared to the small deformation solutions.

We return to the undamped case and show in Fig. 11 the influence of the time step on the calculated vertical displacement time histories of the three subject nodes. Here we utilize the infinitesimal formulation

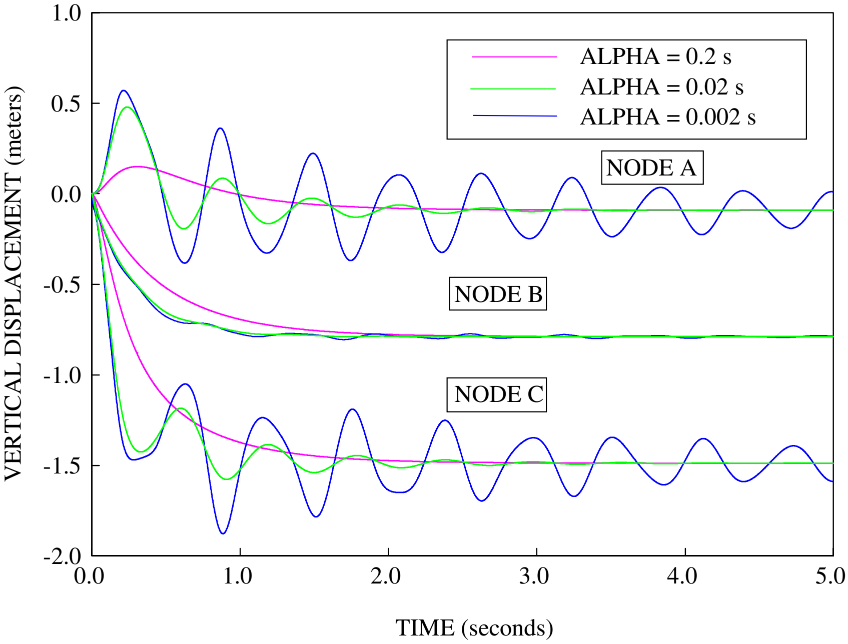

Fig. 9. Porous matrix under partial compression, small deformation analysis: vertical displacement–time histories of surface nodes A, B and C as functions of damping coefficient ALPHA (= α).

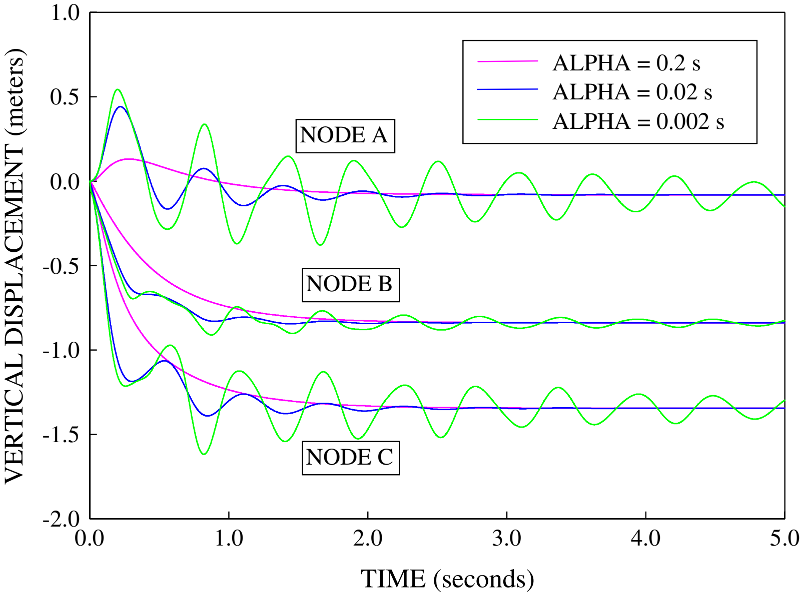

Fig. 10. Porous matrix under partial compression, finite deformation analysis: vertical displacement–time histories of surface nodes A, B and C as functions of damping coefficient ALPHA (= α).

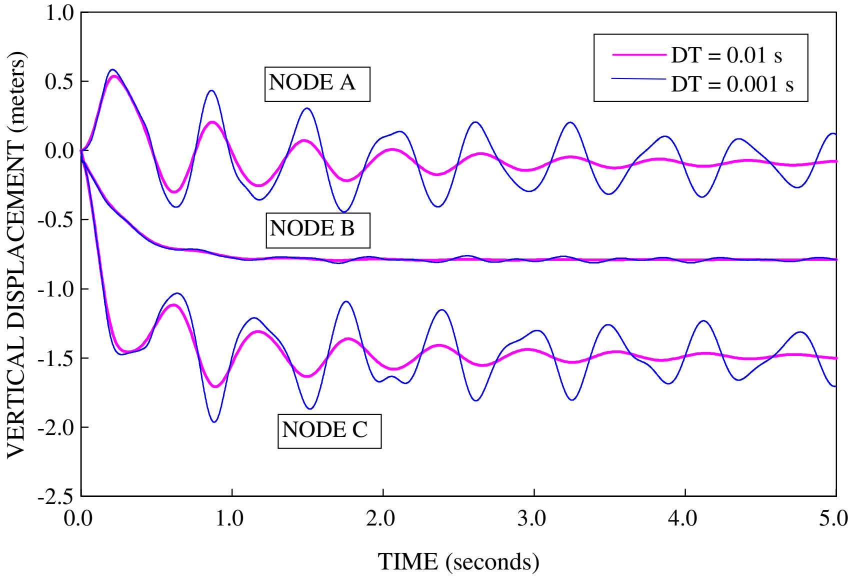

Fig. 11. Porous matrix under partial compression, small deformation analysis: vertical displacement–time histories of surface nodes A, B and C as functions of the time step DT (= Δt).

for illustration purposes and compare the response histories obtained using $\Delta t = 0.01$ s, the 'optimal' time step, and $\Delta t = 0.001$ s, a much refined time step, in the numerical calculations. Note that the time interval between successive reflected waves remains approximately equal to 0.5 s regardless of the time step used. However, the amplitudes and even the shapes of the response curves are greatly affected by the value of the time step. We reiterate that the solution obtained using $\Delta t = 0.01$ s is closer to the true solution of the original partial differential equations, whereas the solution obtained using $\Delta t = 0.001$ s is closer to the solution of the spatially discrete temporally continuous problem.

4.3. Strip footing under harmonic loading

As a final example, we consider a saturated porous foundation supporting a vertically vibrating strip footing. The footing load (in MPa) is given by the harmonic function $w(t) = 3 - 3\cos(\omega t)$, where $\omega = 100$ rad/s is the circular frequency. The footing is 2 m wide, and the porous foundation block is 20 m wide and 10 m deep. Fig. 12 shows the finite element mesh; the left vertical boundary is the plane of symmetry, and hence only the right half of the region is modeled. The boundary conditions on the middle line of the block are applied via horizontal rollers. The upper boundary is free. The left, right and bottom boundaries are supported, and no drainage is allowed. The material parameters are taken as: Lamé constants (in MPa) $\lambda = 8.4$ and $\mu = 5.6$; initial volume fractions $\phi^{s0} = 0.67$ and $\phi^{f0} = 0.33$; reference intrinsic mass densities (in kg/cm^3) $\rho_{s0} = 2500$ and $\rho_{f0} = 1000$; fluid bulk stiffness $K_f = 2.2 \times 10^4$ MPa; hydraulic conductivity $\boldsymbol{k} = \kappa\mathbf{1}$ (isotropic), where κ varies from 0.0001 to 0.1 m/s; and solid matrix damping coefficient $\alpha = 0.02$ s. The time step is taken as $\Delta t = 0.01$ s.

Figs. 13 and 14 show the vertical displacements of node D, located directly below the center of the footing, corresponding to different values of κ as predicted by the small and finite deformation analyses, respectively. We see that the higher the hydraulic conductivity, the higher the response amplitude and

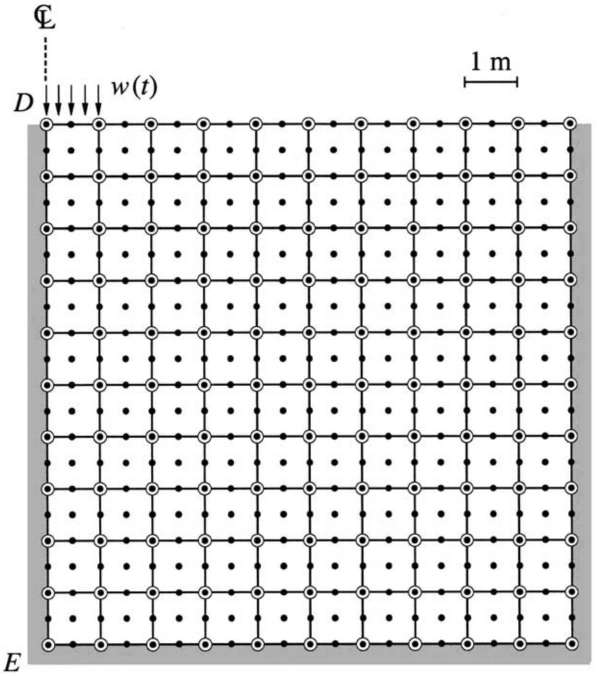

Fig. 12. Strip footing under harmonic loading. Uniform surface pressure $w(t)$ is a harmonic load; vertical sides and bottom boundary are impervious and on roller supports, upper side is a drainage boundary and free.

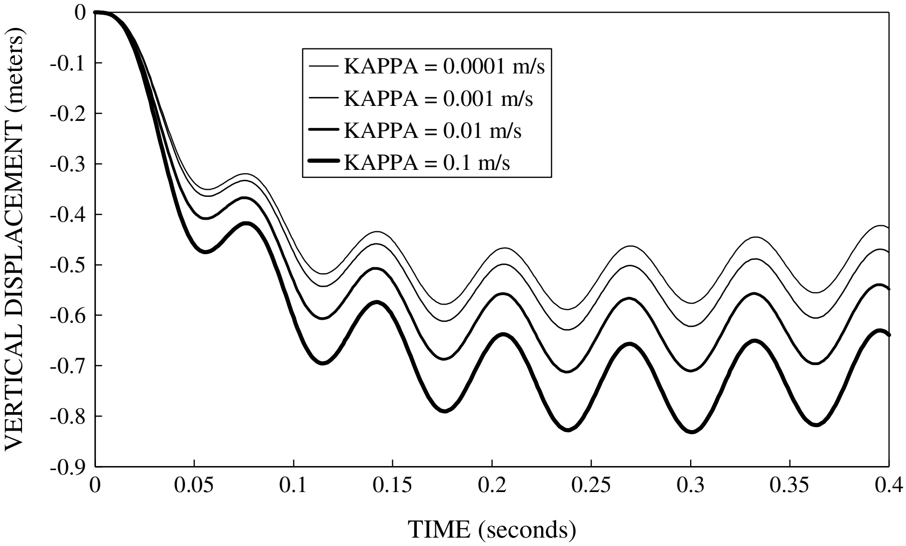

Fig. 13. Strip footing under harmonic loading, small deformation analysis: vertical displacement–time histories of node D as functions of hydraulic conductivity KAPPA ($= \kappa$).

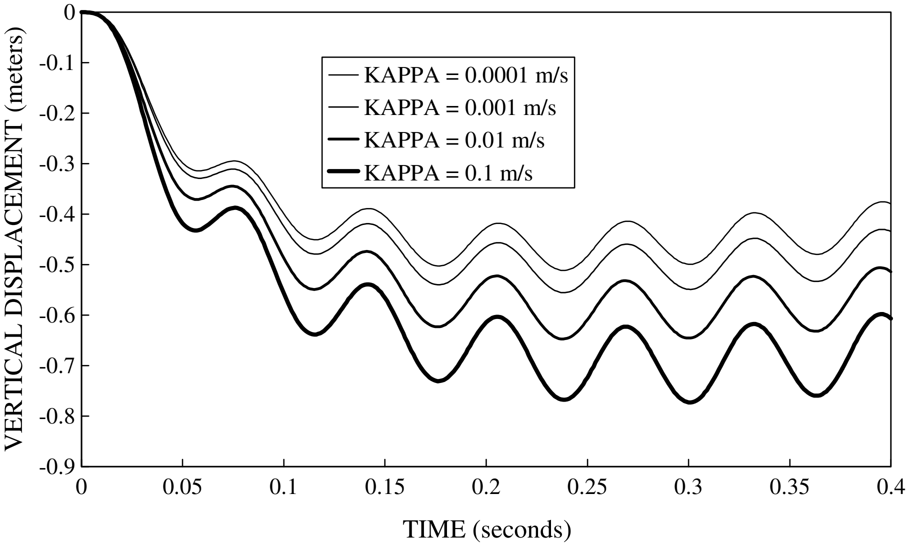

Fig. 14. Strip footing under harmonic loading, finite deformation analysis: vertical displacement–time histories of node D as functions of hydraulic conductivity KAPPA ($= \kappa$).

vertical displacements due to increased drainage and faster compaction of the porous matrix. Figs. 15–18 superimpose these curves for each value of the hydraulic conductivity and demonstrate that the vertical displacements predicted by the small deformation analyses are consistently larger than those predicted by the finite deformation analyses.

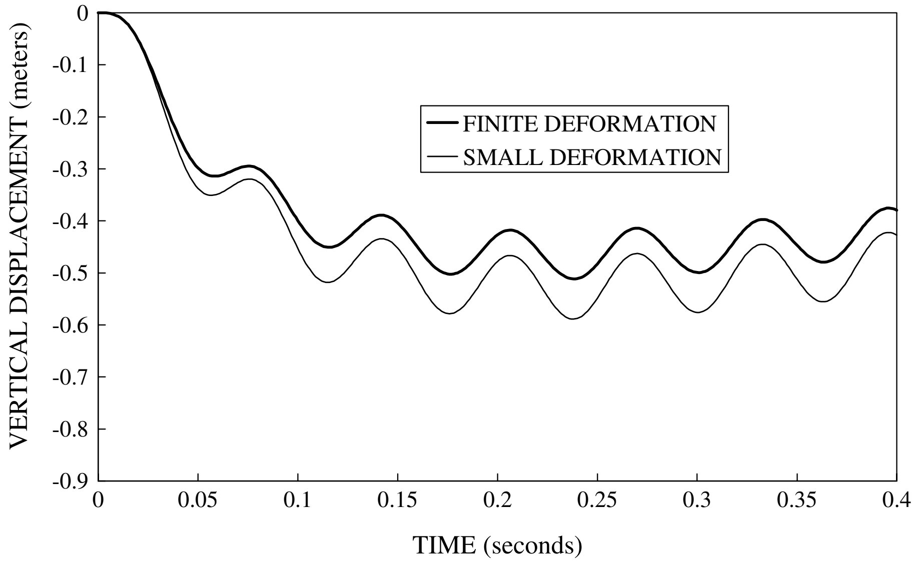

Fig. 15. Strip footing under harmonic loading: vertical displacement–time histories of node D at $\kappa = 0.0001$ m/s.

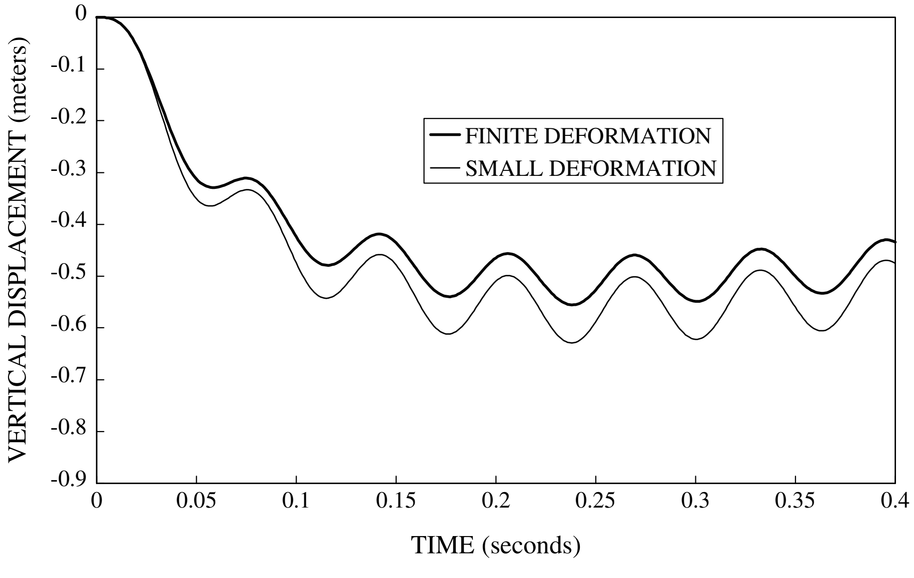

Fig. 16. Strip footing under harmonic loading: vertical displacement–time histories of node D at $\kappa = 0.001$ m/s.

To complete the analysis, we show in Figs. 19–23 the time histories of the excess pore fluid pressure at node E located at the very bottom of the porous block along the centerline of the footing (lower left corner node in Fig. 12). The excess pore fluid pressure in this case is defined as the incremental fluid pressure generated by the application of $w(t)$ on top of the initial hydrostatic value at the beginning of the analysis, and takes on a Cauchy definition. Note in Figs. 19 and 20 that increasing the hydraulic conductivity value

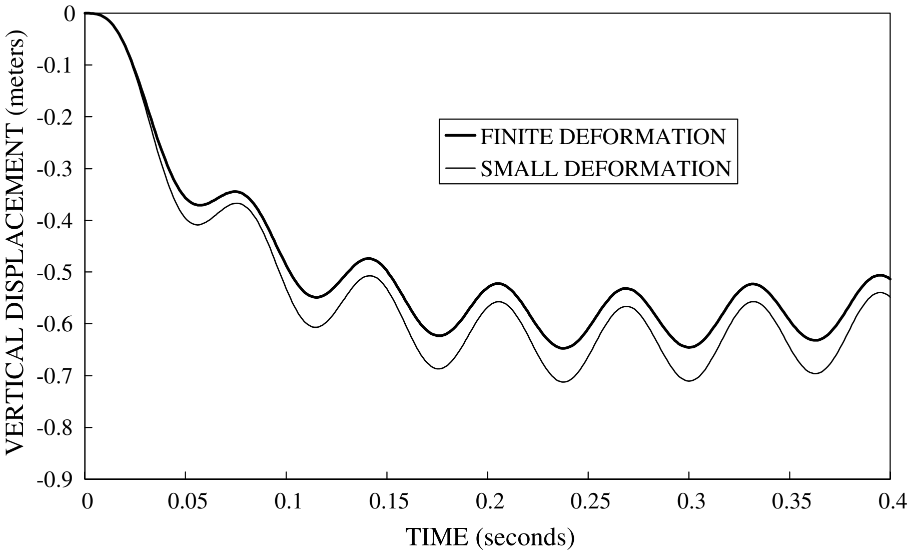

Fig. 17. Strip footing under harmonic loading: vertical displacement–time histories of node D at $\kappa = 0.01$ m/s.

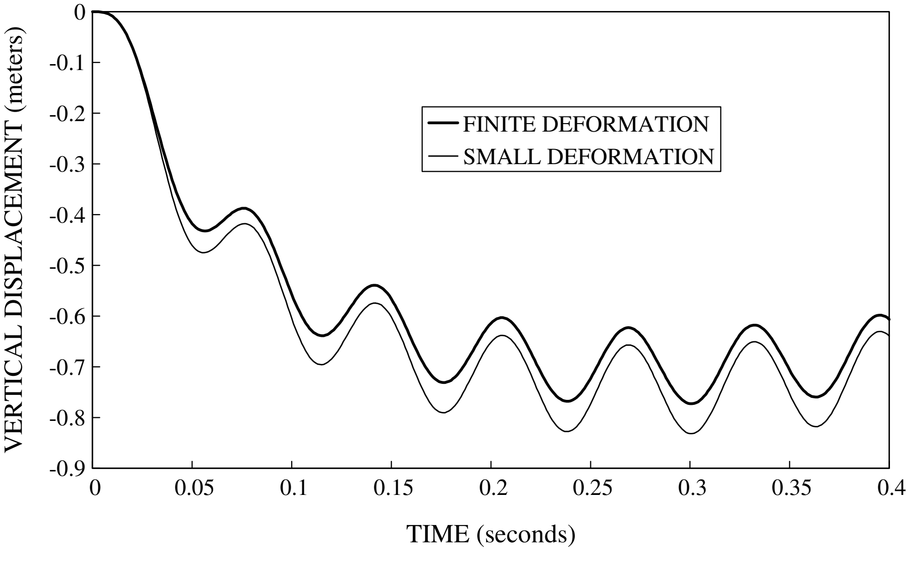

Fig. 18. Strip footing under harmonic loading: vertical displacement–time histories of node D at $\kappa = 0.1$ m/s.

not only produces a phase shift but also causes the excess pore fluid pressure–time histories to oscillate around the value zero due to faster drainage. Figs. 21–23 also show that the amplitudes of the Cauchy excess pore fluid pressure are higher for the finite deformation solutions than for the small deformation solutions. The latter observation could have significant implications on the mathematical simulation of the liquefaction phenomena in saturated granular soils: by neglecting the finite deformation effects the displacements are overestimated while the excess pore fluid pressures are underestimated. This has a com-

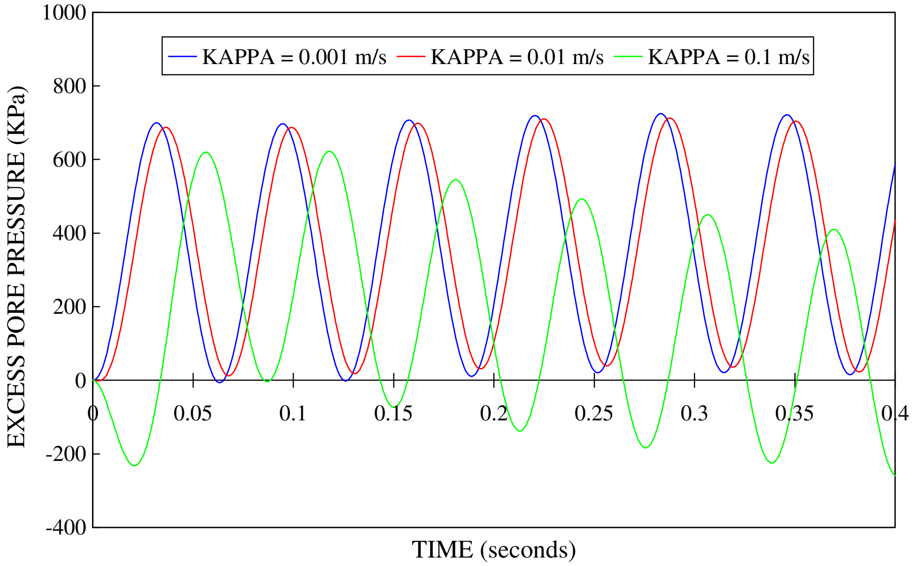

Fig. 19. Strip footing under harmonic loading, small deformation analysis: excess pore fluid pressure–time histories of node E as functions of KAPPA ($=\kappa$).

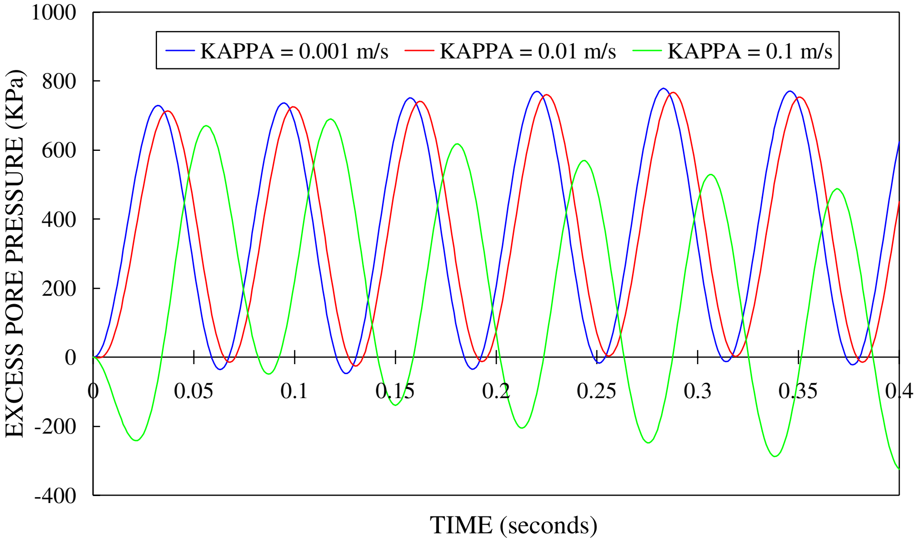

Fig. 20. Strip footing under harmonic loading, finite deformation analysis: excess pore fluid pressure–time histories of node E as functions of KAPPA ($=\kappa$).

pounding effect inasmuch as for the same displacement the small deformation theory could severely underestimate the excess pore fluid pressure buildup, possibly leading to a severe underestimation of the liquefaction susceptibility as well.

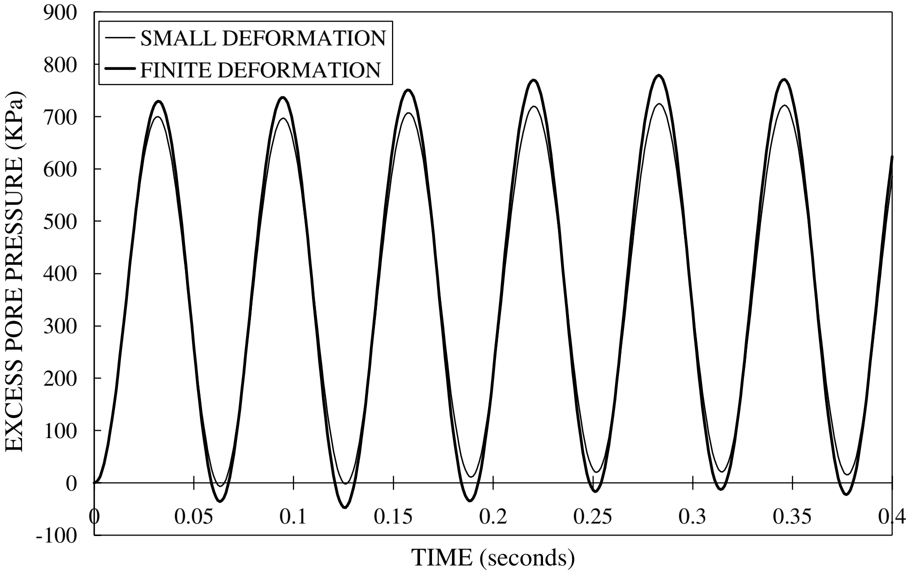

Fig. 21. Strip footing under harmonic loading: excess pore fluid pressure–time histories of node E at $\kappa = 0.001$ m/s.

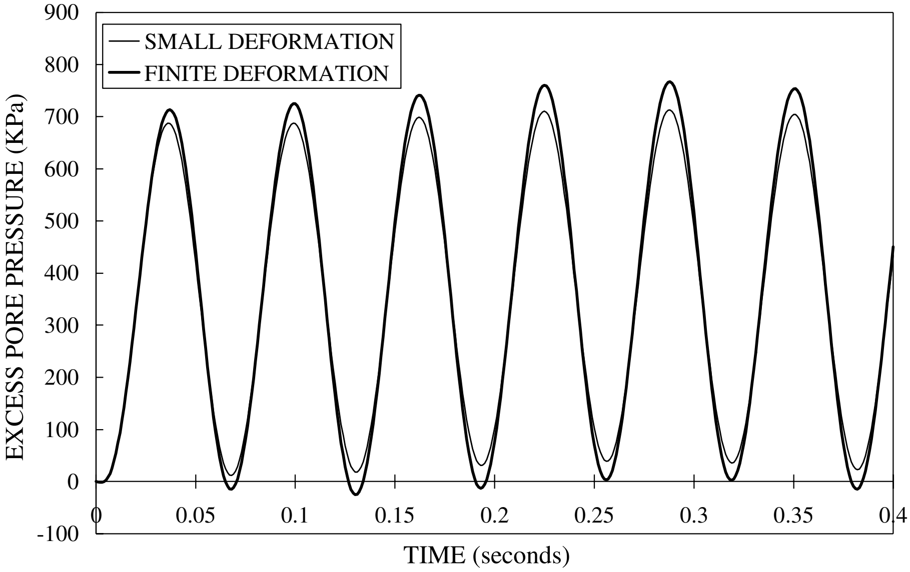

Fig. 22. Strip footing under harmonic loading: excess pore fluid pressure–time histories of node E at $\kappa = 0.01$ m/s.

We conclude this example by showing in Fig. 24 the convergence profile exhibited by the Newton iterations for different time steps. We emphasize that the mixed formulation results in a tangent operator with a large condition number. However, with direct linear equation solving, convergence to a relative error

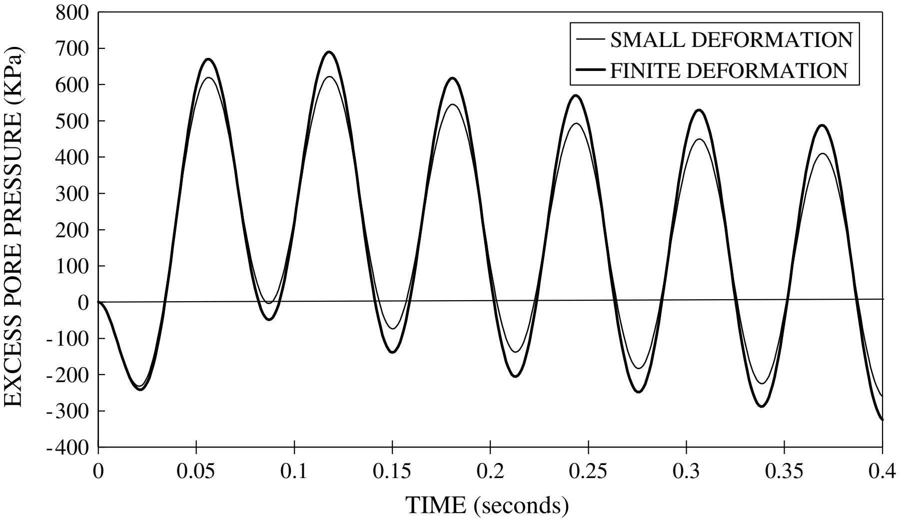

Fig. 23. Strip footing under harmonic loading: excess pore fluid pressure–time histories of node E at $\kappa = 0.1$ m/s.

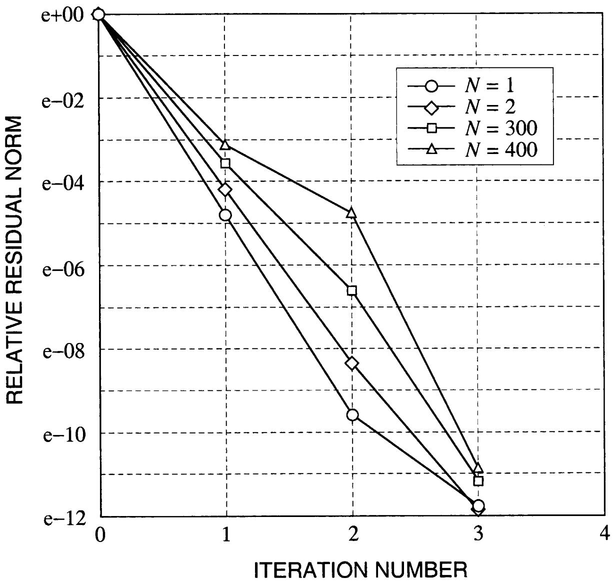

Fig. 24. Strip footing under harmonic loading: convergence profile of global Newton iterations (N = step number).

tolerance of 10^{-10} (relative to the L_2-norm of the residual vector) is very much possible. In fact, even though some of the terms of the tangent operator have been ignored nearly quadratic rate of convergence of the iterations was still achieved. This performance well illustrates the potential of the formulation and the iterative algorithm to accommodate more complex material constitutive models.

5. Summary and conclusions

We have presented a finite element model for the solution of dynamic consolidation of fully saturated porous media in the regime of large deformation. Momentum and mass conservation laws have been written in Lagrangian form by a pull-back from the current configuration to the reference configuration following the solid matrix motion. A complete formulation based on the motion of the solid and fluid phases was first presented; then approximations have been made to arrive at a so-called $(\boldsymbol{v}, p)$-formulation, which is subsequently implemented in a finite element code.

A finite deformation formulation is necessary to accurately predict the transient response of saturated porous media at large strains. Geometrically linear models are not suitable for this purpose since they do not account for the evolving configuration and finite rotation that could have first-order effects on the predicted responses. A specific application example where the proposed finite deformation formulation has been noted to be most useful is the prediction of the liquefaction susceptibility of saturated granular soils since, by neglecting the geometric nonlinearity the liquefaction potential of these materials could be severely underestimated. Other application areas abound in the fields of biomechanics and materials science, among many others, where the underlying physics of porous materials is described by multiphase mechanics.

Acknowledgements

Financial support for this research was provided by National Science Foundation under Contract No. CMS-02-01317 through the direction of Dr. C.S. Astill. Additional funding for the first author was provided by a Stanford Graduate Fellowship through the Civil and Environmental Engineering Department. We thank the two anonymous reviewers for their prompt and constructive reviews.

References

[1] O.C. Zienkiewicz, A.H.C. Chan, M. Pastor, B.A. Schrefler, T. Shiomi, Computational Geomechanics with Special Reference to Earthquake Engineering, John Wiley and Sons, Chichester, 1998.

[2] K. Piekarski, M. Munro, Transport mechanism operating between blood supply and osteocytes in long bones, Nature 269 (1977) 80–82.

[3] L.A. Taber, Biomechanics of growth, remodeling, and morphogenesis, ASME Appl. Mech. Rev. 48 (8) (1995) 487–545.

[4] E.Y.S. Chao, N. Inoue, J.J. Elias, H. Aro, Enhancement of fracture healing by mechanical and surgical intervention, Clin. Orthop. Rel. Res. S355 (1998) S163–S178.

[5] M.L. Knothe-Tate, "Whither flows the fluid in bone?" An osteocyte's perpsective, J. Biomech. 36 (2003) 1409–1424.

[6] H.S. Park, Y.S. Yoon, Application of linear biphasic theory to finite element analysis of head impulse loading, Proc. Inst. Mech. Engrg. Part C—J. Engrg. Mech. Engrg. Sci. 211 (2) (1997) 153–165.

[7] S.C. Cowin, Bone poroelasticity, J. Biomech. 32 (1999) 217–238.

[8] M. Kojic, N. Filipovic, S. Vulovic, S. Mijailovic, A finite element solution procedure for porous medium with fluid flow and electromechanical coupling, Commun. Numer. Methods Engrg. 14 (1998) 381–392.

[9] J.M. Huyghe, D.H. van Campen, T. Arts, R.M. Heethaar, A two-phase finite element model of the diastolic left ventricle, J. Biomech. 24 (1991) 527–538.

[10] J.-K. Suh, R.L. Spilker, M.H. Holmes, A penalty finite element analysis for non-linear mechanics of biphasic hydrated soft tissue under large deformation, Int. J. Numer. Methods Engrg. 32 (1991) 1411–1439.

[11] R.L. Spilker, E.S. de Almeida, P.S. Donzelli, Finite element methods for the biomechanics of soft hydrated tissues: nonlinear analysis and adaptive control of meshes, Cr. R. Biomed. 20 (1992) 279–313.

[12] E.S. Almeida, R.L. Spilker, Finite element formulations for hyperelastic transversely isotropic biphasic soft tissues, Comput. Methods Appl. Mech. Engrg. 151 (1998) 513–538.

[13] M.E. Levenston, E.H. Frank, A.J. Grodzinsky, Variationally derived 3-field finite element formulations for quasistatic poroelastic analysis of hydrated biological tissues, Comput. Methods Appl. Mech. Engrg. 156 (1998) 231–246.

[14] M.E. Levenston, S.R. Eisenberg, A.J. Grodzinsky, A variational formulation for coupled physicochemical flows during finite deformations of charge porous media, Int. J. Solids Struct. 35 (34–35) (1998) 4999–5019.

[15] M. Kojic, N. Filipovic, S. Mijailovic, A large strain finite element analysis of cartilage deformation with electrokinetic coupling, Comput. Methods Appl. Mech. Engrg. 190 (2001) 2447–2464.

[16] J.R. Booker, The consolidation of a finite layer subject to surface loading, Int. J. Solids Struct. 10 (1974) 1053–1065.

[17] J.P. Carter, J.R. Booker, J.C. Small, The analysis of finite elasto-plastic consolidation, Int. J. Numer. Anal. Geomech. 3 (1979) 107–129.

[18] R.W. Lewis, B.A. Schrefler, The finite element method in the static and dynamic deformation and consolidation of porous media, John Wiley and Sons, New York, 1998.

[19] R.I. Borja, One-step and linear multistep methods for nonlinear consolidation, Comput. Methods Appl. Mech. Engrg. 85 (1991) 239–272.

[20] J.T. Christian, Two- and three-dimensional consolidation, in: C.S. Desai, J.T. Christian (Eds.), Numerical Methods in Geotechnical Engineering, McGraw-Hill, San Francisco, CA, 1977, pp. 399–426.

[21] H.J. Siriwardane, C.S. Desai, Two numercial schemes for nonlinear consolidation, Int. J. Numer. Methods Engng. 17 (1981) 405–426.

[22] J.H. Prevost, Implicit-explicit schemes for nonlinear consolidation, Comput. Methods Appl. Mech. Engrg. 39 (1983) 225–239.

[23] J.H. Prevost, Mechanics of continuous porous media, Int. J. Engrg. Sci. 18 (1980) 787–800.

[24] F. Armero, Formulation and finite element implementation of a multiplicative model of coupled poro-plasticity at finite strains under fully saturated conditions, Comput. Methods Appl. Mech. Engrg. 171 (1999) 205–241.

[25] R.I. Borja, E. Alarcón, A mathematical framework for finite strain elastoplastic consolidation. Part1: balance laws, variational formulation, and linearization, Comput. Methods Appl. Mech. Engrg. 122 (1995) 145–171.

[26] R.I. Borja, C. Tamagnini, E. Alarcón, Elastoplastic consolidation at finite strain. Part 2: finite element implementation and numerical examples, Comput. Methods Appl. Mech. Engrg. 159 (1998) 103–122.

[27] J. Larsson, R. Larsson, Non-linear analysis of nearly saturated porous media: theoretical and numerical formulation, Comput. Methods Appl. Mech. Engrg. 191 (2002) 3385–3907.

[28] C.S. Kim, T.S. Lee, S.H. Advani, J.H.W. Lee, Hygrothermomechanical evaluation of porous media under finite deformation: Part II—model validations and field simulations, Int. J. Numer. Methods Engrg. 36 (1993) 161–179.

[29] W. Ehlers, T. Graf, M. Ammann, Deformation and localization analysis of partially saturated soil, Comput. Methods Appl. Mech. Engrg. (in press).

[30] R.I. Borja, Cam-Clay plasticity, Part V: a mathematical framework for three-phase deformation and strain localization analyses of partially saturated porous media, Comput. Methods Appl. Mech. Engrg. (in press).

[31] H.W. Zhang, O.M. Heeres, R. de Borst, B.A. Schrefler, Implicit integration of a generalized plasticity constitutive model for partially saturated soil, Engrg. Computat. 18 (1–2) (2001) 314–336.

[32] O.C. Zienkiewicz, C. Chang, P. Bettess, Drained, undrained, consolidating and dynamic behavior assumptions in soils, Géotechnique 30 (4) (1980) 385–395.

[33] O.C. Zienkiewicz, T. Shiomi, Dynamic behavior of saturated porous media; the generalized Biot formulation and its numerical solution, Int. J. Numer. Anal. Methods Geomech. 8 (1984) 71–96.

[34] J. Ghaboussi, E. Wilson, Variational formulation of dynamics of fluid-saturated porous elastic solids, J. Engrg. Mech. Div., Proc. ASCE 98 (EM4) (1972) 947–963.

[35] M. Kanatani, K. Nishi, M. Kawakami, M. Ohmachi (1988). Two-dimensional nonlinear response analysis during earthquake based on the effective stress method, in: Proceedings of the 6th International Conference on Numerical Methods in Geomechanics, 1988, pp. 1749–1754.

[36] J.H. Prevost, Nonlinear transient phenomena in saturated porous media, Comput. Methods Appl. Mech. Engrg. 20 (1982) 3–18.

[37] J.H. Prevost, J.H., DYNA1-D: A computer program for nonlinear seismic site response analysis, technical documentation. Technical Report NCEER-89-0025, National Center for Earthquake Engineering Research, 1989.

[38] J.C. Simo, T.J.R. Hughes, Computational Inelasticity, Springer, New York, 1998.

[39] J. Bonet, R.D. Woods, Nonlinear Continuum Mechanics for Finite Element Analysis, Cambridge University Press, 1997.

[40] W. Flügge, Viscoelasticity, Springer-Verlag, New York, 1975.

[41] J.C. Simo, Algorithms for static and dynamic multiplicative plasticity that preserve the classical return mapping schemes of the infinitesimal theory, Comput. Methods Appl. Mech. Engrg. 99 (1992) 61–112.

[42] M.A. Biot, General theory of three-dimensional consolidation, J. Appl. Phys. 12 (1941) 155–164.

[43] M.A. Biot, Theory of elasticity and consolidation for a porous anisotropic solid, J. Appl. Phys. 26 (1955) 182–185.

[44] M.A. Biot, Theory of propagation of elastic waves in a fluid–saturated porous solid, J. Acoust. Soc. Am. 28 (1956) 168–191.

[45] M.A. Biot, Mechanics of deformation and acoustic propagation in porous media, J. Appl. Phys. 33 (1967) 1483–1498.

[46] R.J. Atkin, R.E. Craine, Continuum theories of mixtures: basic theory and historical development, Q. J. Mech. Appl. Math. 29 (1976) 209–244.

[47] R.M. Bowen, Theory of mixtures, in: A.C. Eringen (Ed.), Continuum Physics, Mixtures and EM Field Theories, vol. III, Academic Press, New York, 1976, pp. 1–127.

[48] O. Coussy, Mechanics of Porous Continua, Wiley and Sons, New York, NY, 1995.

[49] R. de Boer, Theory of Porous Media, Springer-Verlag, Berlin, Heidelberg, Germany, 2000.

[50] R. de Boer, W. Ehlers, Z. Liu, One-dimensional transient wave propagation in fluid-saturated incompressible porous media, Arch. Appl. Mech. 62 (1993) 59–72.

[51] S. Diebels, W. Ehlers, Dynamic analysis of a fully saturated porous medium accounting for geometrical and material non-linearities, Int. J. Numer. Methods Engrg. 39 (1996) 81–97.

[52] W. Ehlers, S. Diebels, Dynamic deformations in the theory of fluid-saturated porous solid materials, in: Parker, England (Eds.), IUTAM Symposium on Anisotropy, Inhomogeneity and Nonlinearity in Solid Mechanics, Kluwer, Dordrecht, 1995.

[53] L.E. Malvern, Introduction to the Mechanics of a Continuous Medium, Prentice-Hall, Englewood Cliffs, NJ, 1969.

[54] R.I. Borja, Conservation laws for three-phase partially saturated granular media, in: Proceedings of the International Conference from Experimental Evidence Towards Numerical Modelling of Unsaturated Soils, Weimar, Germany, 18–19 September 2003.

[55] J.E. Marsden, T.J.R. Hughes, Mathematical Foundations of Elasticity, Prentice-Hall, Englewood Cliffs, NJ, 1983.

[56] K. Terzaghi, Theoretical Soil Mechanics, Wiley, New York, 1943.

[57] D. Halliday, R. Resnick, J. Walker, Fundamentals of Physics, 6th ed. (extended), John Wiley and Sons, New York, NY, 2001.

[58] T.J.R. Hughes, The Finite Element Method, Prentice-Hall, Englewood Cliffs, NJ, 1987.

[59] C. Li, R.I. Borja, A finite element model of poro-elasticity suitable for large deformation dynamic analysis, John A. Blume Earthquake Engineering Center Report No. 145, Stanford University, California, USA.

[60] J. Bear, Dynamics of Fluids in Porous Media, Dover, New York, 1972.